A Review on Popular Control Applications in Wind Energy Conversion System Based on Permanent Magnet Generator PMSG

Btissam Majout [1], **Houda El Alami** [1], **Hassna Salime** [1], **Nada Zine Laabidine** [1], **Youness El Mourabit** [2], **Saad Motahhir** [3], **Manale Bouderbala** [1], **Mohammed Karim** [1] and **Badre Bossoufi** [1,*]

[1] LIMAS Laboratory, Faculty of Sciences Dhar El Mahraz, Sidi Mohammed Ben Abdellah University Fez, Fez 30050, Morocco
[2] National School of Applied Sciences, Abdelmalek Essaadi University, Tetouan 93000, Morocco
[3] Engineering, Systems and Applications Laboratory, ENSA, SMBA University, Fez 30050, Morocco
* Correspondence: badre.bossoufi@usmba.ac.ma

Abstract: There has always been a high expectation that wind generation systems would capture maximum power and integrate properly with the grid. Utilizing a wind generation system with increased management to meet the growing electricity demand is a clever way of accomplishing this. However, wind power generation systems require a sophisticated, unique, and dependable control mechanism in order to achieve stability and efficiency. To improve the operation of the wind energy conversion method, researchers are continually addressing the obstacles that presently exist. Therefore, it is necessary to know which control can improve the whole system's performance and ensure its successful integration into the network, despite the variable conductions. This article examines wind turbine control system techniques and controller trends related to the permanent magnet synchronous generator. It presents an overview of the most popular control strategies that have been used to control the PMSG wind power conversion system. Among others, we mention nonlinear sliding mode, direct power, backstepping and predictive currents control. First, a description of each control is presented, followed by a simulation performed in the Matlab/Simulink environment to evaluate the performance of each control in terms of reference tracking, response time, stability and the quality of the signal delivered to the network under variable wind conditions. Finally, to get a clear idea of the effect of each control, this work was concluded with a comparative study of the four controls.

1. Introduction

In recent years, all human activities have depended on electrical energy, especially those contributing to economic and social development. This development has led to increased global consumption of electrical energy in recent years [1–3]. According to the latest report by Renewable Energy Policy Network for the 21st Century (REN21, 2015a, p. 27), global energy consumption has been dominated by fossil fuel energy sources (oil, natural gas, and coal), at a level of about 78.3% in 2013. This means that fossil fuels mainly meet energy demand, even though they are the primary source of greenhouse gases (GHG) [2–4]. The presently observed increase in concentrations of these greenhouse gases (GHGs) leads to global warming (Intergovernmental Panel on Climate Change (IPCC), 2007). Many environmental issues result from these climate changes, such as cyclones of unprecedented strength, heat waves, snowstorms, floods, etc. Therefore, preventing the catastrophic consequences of climate change requires the stabilization of the atmospheric concentration of carbon dioxide (CO_2) (IPCC 2007) [4–7].

To deal with this situation, leaders of nations are increasingly turning to renewable energy sources as a solution to meet human needs while preserving the environment [8]. Among renewable energy sources, wind energy has received a significant amount of attention. It is widely used, and has become competitive with conventional energy sources over the last few decades. As a result, the capacity of wind turbines installed worldwide is rising speedily. The World Wind Association forecasts that wind installed capacity can reach 1600 GW by the end of 2030 [9]. Several facts justify the importance given to wind energy, among other renewable energies: it is cost-effective, faster to install, easier to maintain, more reliable, and more efficient. Also, wind farms can be either onshore or offshore [10].

Many structures have been designed in order to implement a wind energy system; for example, there are some equipped with doubly fed induction generators (DFIG's) and squirrel cage induction generators (SCIG's). The only issue with these machines is that they require a multistage gearbox as well as an excitation. For this reason, PMSG has been attracting researchers in recent years due to its higher efficiency and reliability, better performance and its capability to operate at low speed, which eliminates the need for a gearbox; also, this method of control is suitable for low maintenance usage [10,11]. As shown in Figure 1, the machine is mechanically coupled to the blades, and electrically connected to the constant frequency three-phase grid network via a power electronic interface (back-to-back converter). The latter consists of a machine-side converter (MSC) and a grid-side converter (GSC) interconnected through a common DC link with an intermediate capacitor. This structure allows the generator's power to be controlled and adapted to the grid code while operating in fluctuating wind conditions [12,13].
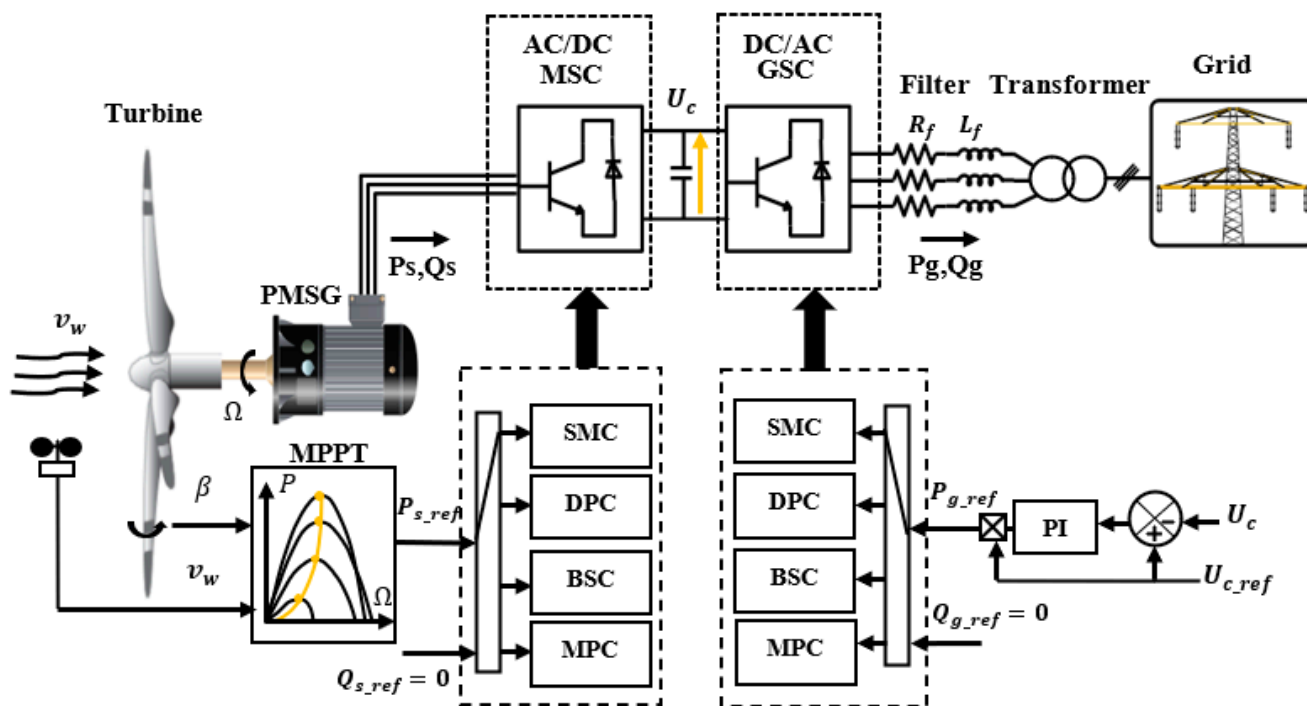
Figure 1. WECS configurations.

In general, the operating region of a wind energy conversion system can be classified into four distinct zones according to the wind speed, as illustrated in Figure 2 [14]. In Zone 1, the system is idle, since the wind speed is too low to start spinning the WT rotor; hence, no power is generated. In Zone 2, the wind speed exceeds the WT's cut-in speed (V_{cut-in}). As a result, the system starts generating power within a range of wind speeds. In this zone, the system is controlled to maximize the produced power given the wind speed variation using the MPPT algorithm, and to reduce the system's oscillation by setting the

pitch angle reference at its optimal value. In Zone 3, the wind speed exceeds the rated speed (V_n). In this case, the WT is controlled by a pitch angle controller to maintain rated power generation during gusty wind speeds. Finally, the wind speed in Zone 4 is more than the cut-out speed ($V_{cut-out}$) of the WT which can cause damage to the wind turbine. In this situation, an emergency device stops the wind turbine to protect it from damage [15].

Figure 2. Different operation zones of a wind turbine.

However, ensuring optimal operation and improving the quality of the power produced by WECS depends not only on the speed control of the PMSG but also on how the back-to-back converters are controlled. Among the control strategies proposed in the literature, vector control (VC) has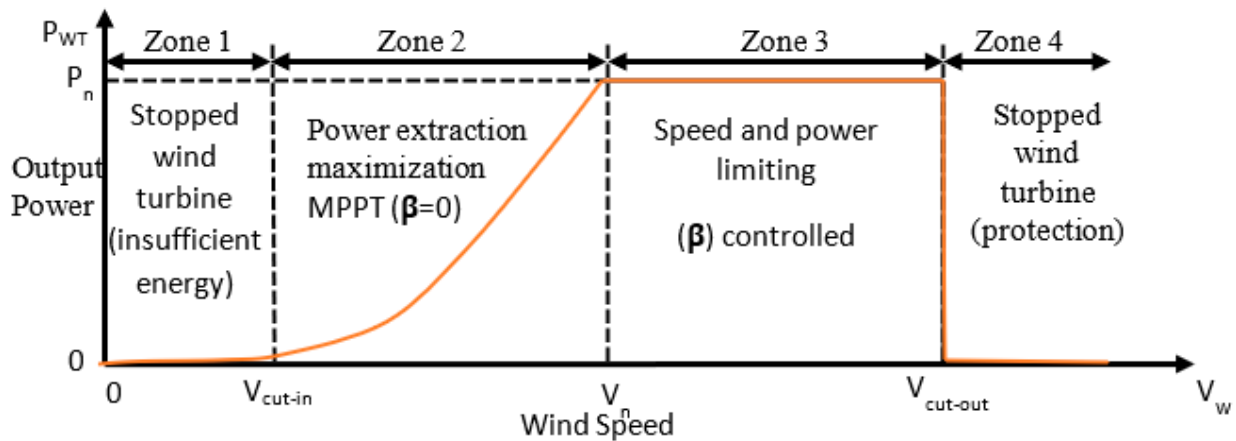 been one of the control strategies used on a large scale to achieve control objectives. This control includes flux-oriented control (FOC) and voltage-oriented control (VOC) methods. Its principle is to make PMSG similar to a direct current machine using the proportional integrator regulator (PI) [16–18]. Nevertheless, the determination of PI gains requires a knowledge of the machine parameters, which makes the control sensitive to the variation of the parameters and thus leads to the deterioration of the system's performance. To eliminate the reliance on machine parameters, Takahashi and Depenbrock proposed the direct power control (DPC), a robust technique that does not require the mathematical model of the system [19]. Unlike other methods, the converter switching states in this control are selected directly from a switching table based on the digital errors between the commanded and estimated values of active and reactive power generated by the hysteresis controllers, without the need for PWM modulation blocks and internal regulation loops. However, despite the numerous benefits of this control, it suffers from variable switching frequency and active and reactive power ripples, which limit the DPC's robustness [20,21].

Other alternatives have been proposed in the literature. As reviewed in [22], SMC is a nonlinear control based on the Lyapunov function. This control is attractive and recommended for many applications. It reduces the complexity of high-order systems to lower-order state variables by forcing the system state trajectory to attain a predesigned sliding surface in finite time and then remain there. However, this control suffers from the chattering phenomena caused by the discontinued term used in the SMC control law.

Meanwhile, Backstepping has piqued the researchers' interest due to its capacity to stabilize the system despite substantial wind variance, which is due to the use of the Lyapunov function in each design step [23]. The principle of this control is to decompose a complex nonlinear system into a sequence of cascaded first-order subsystems where each subsystem acts as a virtual control for the next, which guarantees a good equilibrium state convergence. However, like any other method, this control has its drawbacks. The major one is the "explosion of terms", a flaw created by the repetition of the differentiation of virtual inputs [24].

To address all of these issues, the researchers tried to improve the classical controls by modifying the controllers' designs. These modifications are made by either adding observers, using an adaption mechanism or intelligent techniques (fuzzy logic and neuron network), increasing the controller order, or combining two or more different controllers. However, there is a difficulty with these methodologies in terms of calculation time and practical implementation [25–28]. For this reason, the model predictive control (MPC) has become the most common solution referenced in the past few years due to its simplicity, rapid dynamic response, multivariable control, immediate consideration of non-linear constraints, and ability to be implemented in the electronic boards such as DSpace and FPGA [29,30].

The main contribution of this work is to present a careful overview of the most important techniques that are used to control the PMSG wind power conversion system, varying from classical to modern control design. Therefore, a review of SMC, DPC, BSC, and MPC is given first, followed by the description of the design of these techniques, and finally, the application of the technique on both the machine side and the grid side. Due to the importance of MPPT control in WECS, this study also includes a synthesis of this control. In addition, a simulation test in Matlab/Simulink was performed under a real wind profile to display the effects of each control on the PMSG wind energy conversion system. As a result, this paper can be considered a useful reference that can help new researchers better understand WECS, especially those equipped with permanent magnet synchronous generators, in terms of conception, issues, and control, as well as provoking further research in the wind energy field.

2. Sliding Mode Control

2.1. Review of the Sliding Mode Control

In the late 1950s, Prof. V. I. Utkin and Prof. S. V. Emelyanov described a new sort of nonlinear control based on the Lyapunov function, called sliding mode control (SMC). This control is well-known for its robustness, high accuracy, and simplicity. It can ensure excellent tracking even when the system is subjected to internal parameter fluctuations and external disturbances [31,32]. Other than PMSG-based wind power systems, SMC has been successfully applied in many different wind power system structures [33–38]. This control is considered an effective way to transform a relatively high-order system into a lower-order system, which facilitates the controller design, since there is much knowledge in the literature on designing control and analyzing stability for low-order systems. Its principle is to alter the dynamics of the nonlinear system by applying a discontinuous control signal that forces the system to lie on the prescribed sliding surface of the system's normal behavior [39]. However, the basic SMC configuration suffers from the steady chattering phenomenon induced at the steady state [40] due to the discontinuous term used in the SMC structure. This phenomenon causes the system response to chatter, leading to high degradation in the system performance and affecting the quality of the injected current (high THD) [41–43]. Therefore, there was a need to develop the conventional SMC design to overcome this issue. Many researchers attempted to overcome the chattering problem by proposing several new SMC configurations [44,45]. The following figure shows the improved control structures of SMC that have been proposed to improve the conventional SMC (Figure 3).
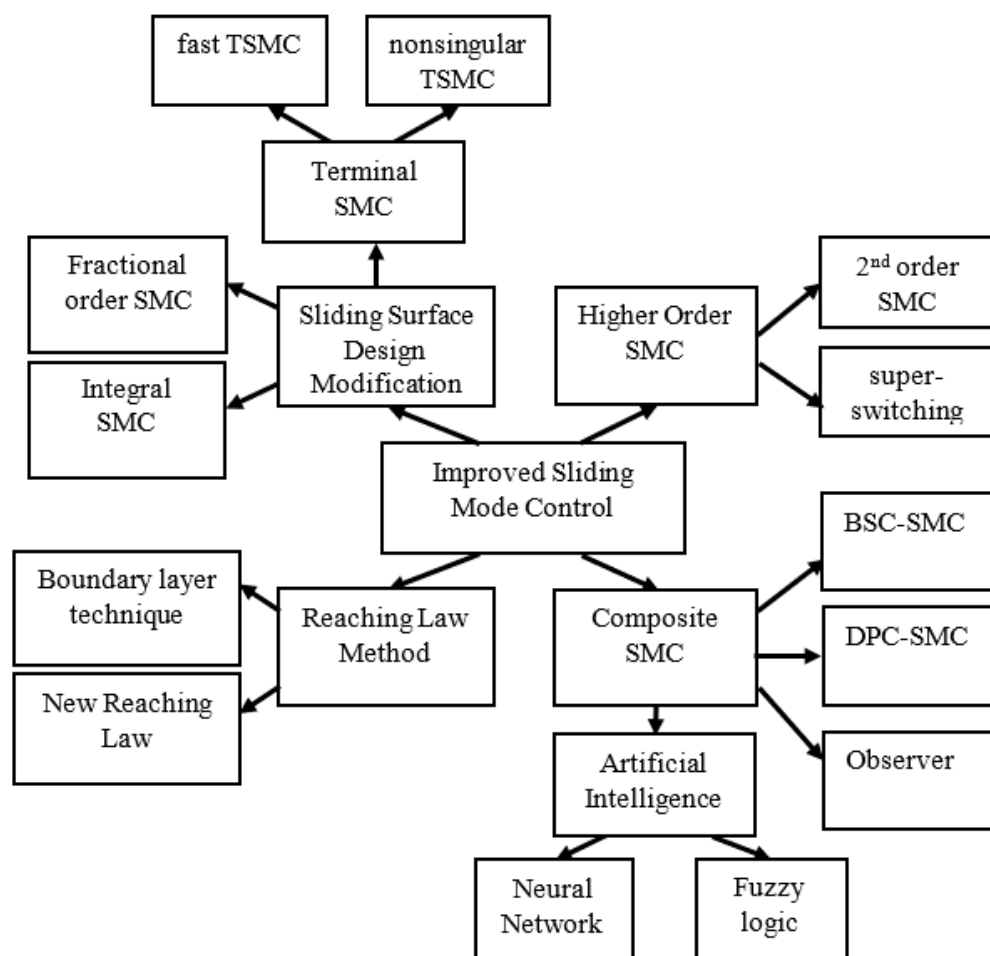
Figure 3. Summary of SMC enhancement techniques.

Among all sorts of suggested methods that have attempted to improve the first-order SMC, the high-order SMC control has received much attention in recent years due to its prominent advantages [38]. The main idea of this control is to reduce the chattering phenomenon and at the same time to preserve the advantages of the original approach; by acting on the higher-order time derivatives of the system's deviation from the constraint instead of influencing the first derivative of the deviation as it happens in the standard sliding modes. Based on the several references, the most successful version of the HOSMC is the super-twist algorithm. Its high performance was shown in a variety of industrial applications [44,46,47].

The terminal SMC (TSMC) scheme is also a class of SMC [48–54]. Unlike HOSMC, the basic idea of this control is to achieve finite-time system convergence with a minimum output control level by using fractional order terms [51]. However, the fractional-order terms in the sliding manifold cause a singularity problem in this method, affecting the system's stability. More advanced versions of this control are proposed to address the singularity problem and accelerate the convergence of the basic TSMC, such as the nonsingular TSMC [49–51] and the fast TSMC [52–55]. Meanwhile, the authors in [56] attempted to extend SMC by adding an integral action to the sliding surface. This integral term forces the system to start on the manifold at the initial condition and constrains it during the entire closed-loop response of the system. As a result, the chattering phenomena are reduced. However, to ensure a good balance between robustness and chattering phenomena, this control requires sufficient skill to adjust the controller gain parameters [57,58].

Other techniques have been used to suppress the chattering problem, such as adaptive SMC [59–62], perturbation observer-based sliding-mode control [63,64], and predictive sliding mode control [65] and reaching law SMC [66,67]. This last technique consists in

replacing the discontinuous function "Sign" used on the sliding mode control design with other mathematical functions such as the saturation function, hyperbolic tangent function, and exponential function [68–71].

Besides all the previous proposed techniques and for the same purpose, another method for designing the SMC controller, called "hybridization", has been proposed in the literature. This method consists of combining the SMC with other techniques [59,72]. In [59], Lin & Chen used genetic algorithms to optimize the SMC and FLC combination and thus reduce the "chattering" phenomenon in the system. In [73,74], the authors combined the sliding mode control and the H∞. This technique was used to define the sliding mode attractive control part, which is the primary cause of the chattering phenomena.

On the other hand, literature [75] proposes a combination of SMC with other nonlinear control called "backstepping" to optimize a linear induction machine performance. As described, this suggestion was validated through field-programmable gate array (FPGA). This approach was later successfully applied in a variable-speed wind turbine power system [63], providing good results under fluctuating wind speeds. Elsewhere, literature [64] presented sliding mode-based direct power control to control wind power systems under unbalanced grid voltage conditions, and literature [70–76] wisely chose to integrate SMC with artificial neural networks.

Table 1 summarizes the different techniques used for SMC control that are found in the literature.

Table 1. Various techniques used for SMC control.

	Techniques	Researchers
Sliding Mode Control	Hight order	Valenciaga F et al. [38]
	Second order	Matraji I et al. [39]; Benbouzid M et al. [40]; Xiaoning S et al. [41]; Benelghali S et al. [42]
	Super twisting	Phan D et al. [43]; Zholtayev D et al. [44]; Yaichi I et al. [45];
	Terminal	Shihua L et al. [48];
	Integral	Saravanakumar R et al. [56]; Jun Liu et al. [57]; Muhammad M et al. [58];
	H∞ technique	Kharabian B et al. [60]; Lian J et al. [61];
	Backstepping-SMC	Faa-Jeng L et al. [62]; Rajendran S et al. [63];
	Direct power control	Shang L et al. [64]; Benbouhenni H et al. [65];
	Fuzzy logic	Diab A. A. Z et al. [66]; Yin, X.-X et al. [67]; El Karaoui I et al. [68]; Saghafinia A et al. [69];
	Artificial neural network	Hong C-M et al. [70]; Mohammad B et al. [71];
	Adaptive model	Baek S et al. [72]; Ton Hoang Nguyen et al. [73];
	Observer	Kim H et al. [77]; Mi Y et al. [78–80];
	Reaching law	Mozayan S. M et al. [81]; Fallaha, C.J. et al. [82]; El Makrini I et al. [83]

2.2. Application of Sliding Mode Control on the PMSG Wind Power System

The sliding surface used in this study is as follows [31]:

$$S(x) = \left(\frac{d}{dt} + \delta\right)^{n-1} \times e(x) \tag{1}$$

$S(x)$ represents the sliding surface proposed by J. SLOTINE. Variable n is the order of the system, δ is a positive constant, and $e(x)$ is the error between the desired signal x_{ref} and the state variable x [32]. With $n = 1$, the tracking error dynamics of the proposed sliding surface become:

$$S(x) = e(x) = x_{ref} - x \tag{2}$$

To attain a commutation around the surface, the equivalent SMC formula $u(t)$ is developed as the addition of two expressions (see Figure 4). Term u_{eq} is an equivalent control that characterizes the system's behavior on the sliding surface, while u_n is a switching control based on a discontinuous function. This latter is employed to satisfy the conditions of attractiveness and stabilization [37]. Therefore, the sliding mode control law can be presented as:

$$u(t) = u(t)_{eq} + u(t)_n \tag{3}$$

With,

$$u_n = K_n\, sgn(S_n) \tag{4}$$

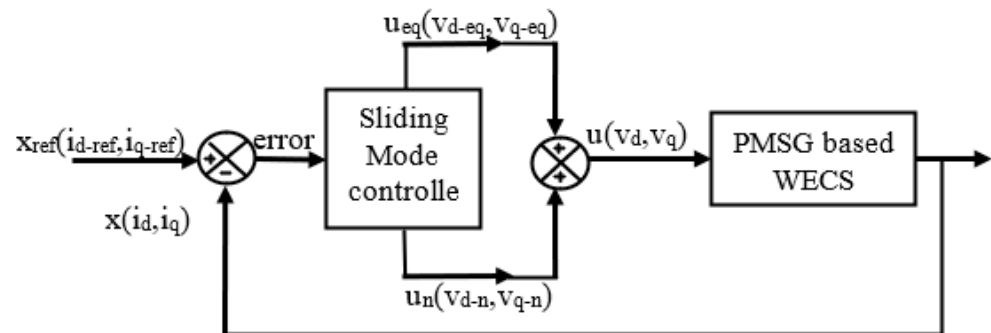K_n is a switching gain, and $sgn(S_n)$ is a discontinuous mathematical function.

Figure 4. SMC controller structure.

This section aims to determine the switching control inputs for the MSC and GSC. During this process, the controller design of each side will be built systematically, as explained below.

2.2.1. Machine-Side Control

The chosen surfaces that were used to control the machine-side converter MSC are as follows:

$$\begin{cases} S(i_{sd}) = e(i_{sd}) = i_{sd\_ref} - i_{sd} \\ S(i_{sq}) = e(i_{sq}) = i_{sq\_ref} - i_{sq} \end{cases} \tag{5}$$

The chosen surfaces' derivatives are as follows:

$$\begin{cases} \dot{S}(i_{sd}) = \frac{di_{sd\_ref}}{dt} - \frac{di_{sd}}{dt} \\ \dot{S}(i_{sq}) = \frac{di_{sq\_ref}}{dt} - \frac{di_{sq}}{dt} \end{cases} \tag{6}$$

Replacing $\frac{di_{sd}}{dt}$ and $\frac{di_{sq}}{dt}$ with their expression given by Equation (A6) in Appendix A, respectively, in Equation (6) gives:

$$\begin{cases} \dot{S}(i_{sd}) = \frac{di_{sd\_ref}}{dt} + \frac{R_s}{L_{sd}} \cdot i_{sd} - p \cdot \Omega \cdot \frac{L_{sq}}{L_{sd}} \cdot i_{sq} - \frac{V_{sd}}{L_{sd}} \\ \dot{S}(i_{sq}) = \frac{di_{sq\_ref}}{dt} + \frac{R_s}{L_q} \cdot i_{sq} + p \cdot \Omega \cdot \frac{L_{sd}}{L_{sq}} \cdot i_{sd} + p \cdot \Omega \cdot \frac{\varnothing_f}{L_{sq}} - \frac{V_{sq}}{L_{sq}} \end{cases} \tag{7}$$

Replacing v_{sdq} with $\left(v_{sdq\_eq} + v_{sdq\_n}\right)$ in Equation (7) gives:

$$\begin{cases} \dot{S}(i_{sd}) = \frac{di_{sd\_ref}}{dt} + \frac{R_s}{L_{sd}} \cdot i_{sd} - p \cdot \Omega \cdot \frac{L_{sq}}{L_{sd}} \cdot i_{sq} - \frac{\left(v_{sd\_eq} + v_{sd\_n}\right)}{L_{sd}} \\ \dot{S}(i_{sq}) = \frac{di_{sq\_ref}}{dt} + \frac{R_s}{L_{sq}} \cdot i_{sq} + p \cdot \Omega \cdot \frac{L_{sd}}{L_{sq}} \cdot i_{sd} + p \cdot \Omega \cdot \frac{\varnothing_f}{L_{sq}} - \frac{\left(v_{sq\_eq} + v_{sq\_n}\right)}{L_{sq}} \end{cases} \tag{8}$$

The control principles are clearly shown in the Equation (8).

During the sliding mode and in the steady-state, $\dot{S}(x) = 0$ and $v_{sdq\_n} = 0$. Therefore, the expression of the equivalent control components v_{sdq_eq} can be deduced from Equation (8) as follows:

$$\begin{cases} v_{sd\_eq} = L_{sd}\left[\frac{di_{sd\_ref}}{dt} + \frac{R_s}{L_{sd}}\cdot i_{sd} - p\cdot\Omega\cdot\frac{L_{sq}}{L_d}\cdot i_{sq}\right] \\ v_{sq\_eq} = L_{sq}\left[\frac{di_{sq\_ref}}{dt} + \frac{R_s}{L_{sq}}\cdot i_{sq} + p\cdot\Omega\cdot\frac{L_{sd}}{L_{sq}}\cdot i_{sd} + p\cdot\Omega\cdot\frac{\varnothing_f}{L_{sq}}\right] \end{cases} \tag{9}$$

Whereas v_{sdq_n} is given by the following equations:

$$\begin{cases} v_{sd\_n} = K_d\cdot sign(S(i_{sd})) \\ v_{sq\_n} = K_q\cdot sign(S(i_{sq})) \end{cases} \tag{10}$$

As explained previously, each control approach component should be calculated by adding two terms $\left(v_{sdq\_eq} + v_{sdq\_n}\right)$. Therefore, the MSC controller becomes as follows:

$$\begin{cases} v_{sd} = L_{sd}\left[\frac{di_{sd\_ref}}{dt} + \frac{R_s}{L_{sd}}\cdot i_{sd} - p\cdot\Omega\cdot\frac{L_{sq}}{L_{sd}}\cdot i_{sq}\right] + K_{sd}\cdot sign(S(i_{sd})) \\ v_{sq} = L_{sq}\left[\frac{di_{sq\_ref}}{dt} + \frac{R_s}{L_{sq}}\cdot i_{sq} + p\cdot\Omega\cdot\frac{L_{sd}}{L_{sq}}\cdot i_{sd} + p\cdot\Omega\cdot\frac{\varnothing_f}{L_{sq}}\right] + K_{sq}\cdot sign(S(i_{sq})) \end{cases} \tag{11}$$

In this study, the direct current reference i_{sd_ref} is set to zero to maximize the electromagnetic torque T_{em}, while the quadrature current reference i_{sq_ref} is derived from the speed controller. Hence, the i_{sq_ref} expression can be presented as:

$$i_{sq\_ref} = i_{sq\_ref\_eq} + i_{sq\_ref\_n} \tag{12}$$

$$i_{sq\_ref} = -\frac{2}{3}\cdot\frac{J_{tot}}{p\cdot\varnothing_f}\left[\dot{\Omega}_{ref} + \frac{f}{J_{tot}}\cdot\Omega - \frac{1}{J_{tot}}\cdot T_{turb}\right] + K_\Omega\cdot sign(S(\Omega)) \tag{13}$$

where Ω_{ref} is deduced from the MPPT control strategy (Figure 5).
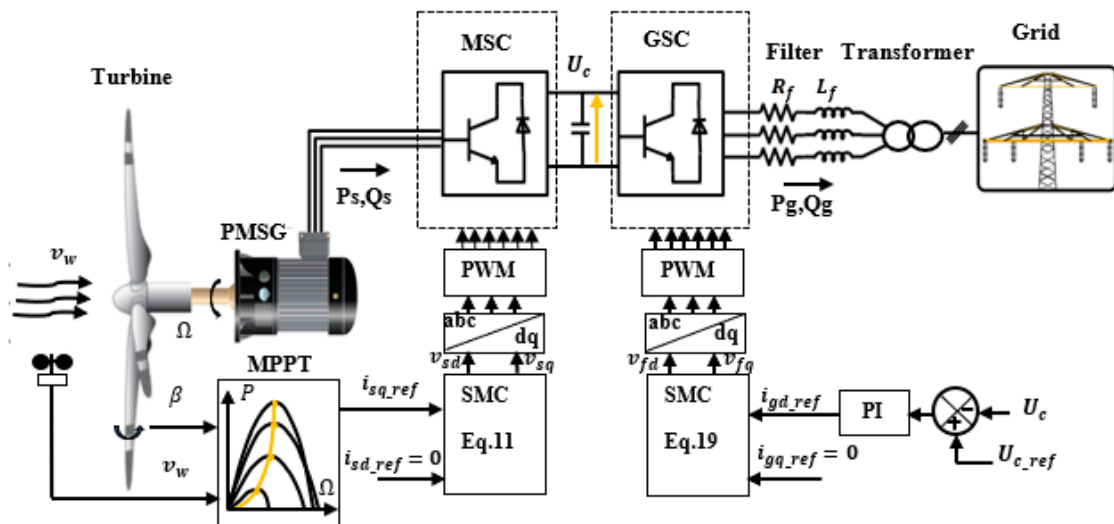
Figure 5. SMC applied to the PMSG-WECS.

2.2.2. Grid-Side Control

The grid-side converter maintains a constant capacitor voltage and adjusts the *d*-axis and *q*-axis currents frequency, thus ensuring good power transmission into the grid [36]. Therefore, two sliding mode controllers have been designed to control GSC's components (i_{gd}, i_{gq}) (Figure 5).

The following equations present the sliding surfaces chosen to control this side:

$$\begin{cases} S\left(i_{gd}\right) = e\left(i_{gd}\right) = i_{gd\_ref} - i_{gd} \\ S\left(i_{gq}\right) = e\left(i_{gq}\right) = i_{gq\_ref} - i_{gq} \end{cases} \tag{14}$$

Terms i_{g_ref} and i_{gd_ref} are the direct and the quadrature grid currents references, respectively.

The grid side converter controller (GSC) can be designed using a mechanism similar to that used to control the machine side converter (MSC).

$$v_{fd} = v_{fd\_eq} + v_{fd\_n} \tag{15}$$

$$v_{fq} = v_{fq\_eq} + v_{fq\_n} \tag{16}$$

With,

$$\begin{cases} v_{fq\_eq} = L_f\left[\frac{di_{gd\_ref}}{dt} + \frac{R_f}{L_f}\cdot i_{gd} - w_g\cdot i_{gq} + \frac{V_{gd}}{L_f}\right] \\ v_{fq\_n} = K_{fd}\cdot sign\left(S\left(i_{gd}\right)\right) \end{cases} \tag{17}$$

$$\begin{cases} v_{fq\_eq} = L_f\left[\frac{di_{gq\_ref}}{dt} + \frac{R_f}{L_f}\cdot i_{gq} + w_g\cdot i_{gd} + \frac{V_{gq}}{L_f}\right] \\ v_{fq\_n} = K_{fq}\cdot sign(S(i_{gq})) \end{cases} \tag{18}$$

Hence, the GSC controller becomes as follows:

$$\begin{cases} v_{fd} = L_f\left[\frac{di_{gd\_ref}}{dt} + \frac{R_f}{L_f}\cdot i_{gd} - w_g\cdot i_{gq} + \frac{V_{gd}}{L_f}\right] + K_{fd}\cdot sign\left(S\left(i_{gd}\right)\right) \\ v_{fq} = L_f\left[\frac{di_{gq\_ref}}{dt} + \frac{R_f}{L_f}\cdot i_{gq} + w_g\cdot i_{gd} + \frac{V_{gq}}{L_f}\right] + K_{fq}\cdot sign(S(i_{gq})) \end{cases} \tag{19}$$

where i_{gq_ref} is deduced from the reactive power Q_{g_ref} the expression which is fixed to zero to achieve a unity power factor control, while i_{gd_ref} is generated by the dc-link voltage regulator, as shown in Figure 5. Figure 5 illustrates the general structure of SMC within the PMSG-wind energy conversion system.

The SMC controllers' stability in both MSC and GSC was examined using a Lyapunov stability analysis. Therefore, two Lyapunov functions (V_{MSC}, V_{GSC}) were chosen for this study.

$$\begin{cases} V_{MSC} = \frac{1}{2}(S_{i_{sd}}^2 + S_{i_{sq}}^2 + S_{\Omega}^2) \\ V_{GSC} = \frac{1}{2}(S_{i_{gd}}^2 + S_{i_{gq}}^2) \end{cases} \tag{20}$$

where V_{MSC} was used for the MSC, whereases V_{GSC} was used for the GSC.

To achieve stability with Lyapunov function, the switching gains ($K_{\Omega}, K_{sd}, K_{sq}, K_{fd}$ and K_{fq}) that are used in the switching control must be set to positive values while the derivative function should be negative ($\dot{V}_{MSC} < 0\ \dot{V}_{GSC} < 0$). Functions V_{MSC} and V_{GSC}'s time derivatives are as follows:

$$\begin{cases} \dot{V_{MSC}} = S_{i_{sd}}\cdot\dot{S}_{i_{sd}} + S_{i_{sq}}\cdot\dot{S}_{i_{sq}} + S_{\Omega}\cdot\dot{S}_{\Omega} < 0 \\ \dot{V_{GSC}} = S_{i_{gd}}\cdot\dot{S}_{i_{gd}} + S_{i_{gq}}\cdot\dot{S}_{i_{gq}} < 0 \end{cases} \tag{21}$$

Replacing each surface $\dot{S}(x)$ with its expression in Equation (21) gives:

$$\begin{cases} \dot{V_{MSC}} = -K_d\cdot S_{i_{sd}}\cdot sign(S(i_{sd})) - K_q\cdot S_{i_{sq}}\cdot sign(S(i_{sq})) - K_{\Omega}\cdot S_{\Omega}\cdot sign(S(\Omega)) \\ \dot{V_{GSC}} = -K_{fd}\cdot S_{i_{gd}}\cdot sign\left(S\left(i_{gd}\right)\right) - K_{fq}\cdot S_{i_{gq}}\cdot sign(S(i_{gq})) \end{cases} \tag{22}$$

Replacing $sign(S(x))$ with its expression in Equation (22) gives:

$$\begin{cases} \dot{V}_{MSC} = -K_\Omega \cdot |S_\Omega| - K_d \cdot \left|S_{i_{sd}}\right| - K_q \cdot \left|S_{i_{sq}}\right| \\ \dot{V}_{GSC} = -K_{fd} \cdot \left|S_{i_{gd}}\right| - K_{fq} \cdot \left|S_{i_{gq}}\right| \end{cases} \tag{23}$$

When K_Ω, K_{sd}, K_{sq}, K_{fd} and K_{fq} are positive constants, the $\dot{V}_{MSC}$ and $\dot{V}_{GSC}$ are negative. Hence, the Lyapunov condition is satisfied, and the proposed control's objectives are achieved.

3. Direct Power Control

3.1. Review of Direct Power Control

The principle of direct power control (DPC) was first developed by "T.Ohnishi" [84]. A few years later, the DPC control was advanced by researchers "Noguchi" and "I.Takahachi" [85]. The active and reactive power control is guaranteed using an instantaneous power control loop to ensure the decoupling between the two powers while providing a unity power factor [86].

Over the years, researchers have used DPC in different modes where control algorithms can be classified under two broad categories: virtual flux-based DPC and voltage-based DPC. Early DPC commands were based on predefined switching tables and hysteresis controllers. Depending on the outputs of these controllers, the switching states of the different power converters can be realized, which leads to the desired active and reactive power generation. In addition, the determination of the flux vectors [87–90] and the synchronization with the grid voltage [91–96] have been elaborated through the predefined switching tables. The major disadvantage of DPC based on switching tables lies in the high sampling frequency required in order to obtain relatively satisfactory performance. We can also add the undesirable effect of the variable switching frequency on the total harmonic distortion (THD). Indeed, the THD in this kind of control using hysteresis controllers remains considerably high compared to other control algorithms.

The diagram in the following figure illustrates the different control algorithms based on the DPC principle, either for the voltage-based DPC or the virtual flux-based DPC (Figure 6).
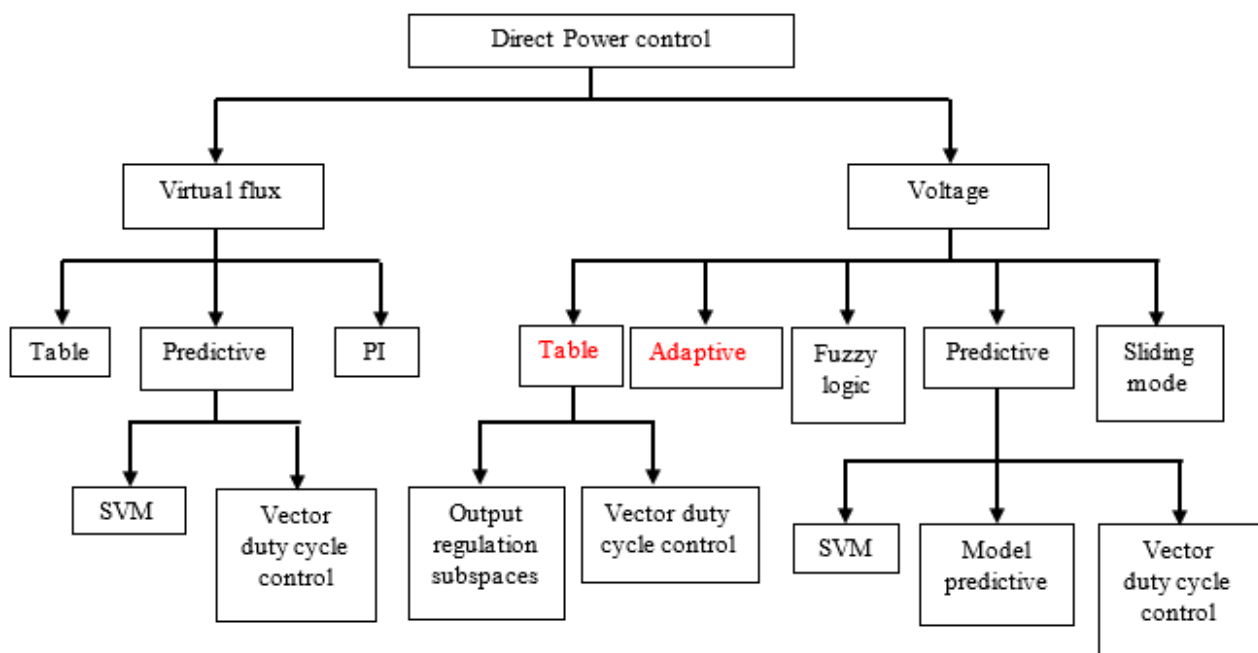

Figure 6. Different control strategies based on the DPC principle.

As discussed previously, the predictive control of the model became the most employed algorithm in the DPC strategy, based on either the voltage or the virtual flow [84–89]. The precision and efficiency of the DPC control that adapts the predictive model remains superior compared to the DPC that uses predefined vector selection tables. The major problem of the DPC control based on the predictive model resides in the variable switching frequency of the power converters. Nevertheless, studies have been performed incorporating modulation blocks into the design of control algorithms to achieve symmetrical and constant switching frequencies to minimize the undesirable effects of variable switching frequencies. These solutions employ sequences of vectors synchronized via well-defined sampling periods. However, the algorithms employed in these solutions require a more complex calculation than do the traditional algorithms.

Predictive DPC can be subdivided into two broad categories, namely, predictive DPC based on vector duty cycle control [97–99] and predictive DPC based on spatial vector modulation (SVM) [100]. The SVM technique requires a referential transformation to present the virtual flux and the grid voltage to offer the sequence and the duration of the vectors applied to the converter. In addition, it requires a powerful calculator that makes it possible to put the various complex operations in force [101–112].

It should be noted that there are also other techniques used for voltage-based DPC control, such as sliding mode [113–116], fuzzy logic [117,118], and adaptive technique [119,120]. However, these latter techniques require sophisticated computational resources for their implementation. A technique that does not require this kind of robust computation is the DPC technique based on the proportional-integral (PI) regulator with the SVM technique proposed by Malinowski et al. [121]. However, the design requires additional parameterization to calculate the PI controller gains.

In addition, the various techniques employed for DPC control tend to minimize undesirable defects, improving the performance demonstrated by DPC control. The key points required for these control techniques are minimization of ripples due to the use of electronic switches and the reduction of the total harmonic distortion (THD) of electric currents. However, the techniques discussed above consider that the supply voltage is purely balanced and sinusoidal, which is unrealistic in the presence of static converters. Therefore, authors in [122,123] have attempted to study the behavior of the DPC control under unfavorable conditions regarding wave distortion and supply voltage imbalance. The techniques "output regulation subspaces" (ORS) [122] and "vector duty cycle control" (VDC) [123] are used starting from the control based on predefined tables and using the technique of the voltage-based DPC.

The DPC technique used under unfavorable conditions is significantly less present in the literature. For example, the operation under an unbalanced supply voltage is presented in the studies [124–127], where the extraction of the virtual flux and grid current parameters becomes complicated. On the other hand, authors in [94,119] attempted to extend DPC by employing the p-q extension theory mentioned in [128].

Table 2 summarizes the different techniques used for the DPC control found in the literature.

Table 2. Various techniques used for DPC control.

Techniques		Researchers
Virtual flux	Proportional-Integral PI	Malinowski M et al. [121]
	Vector Duty Cycle Control Predictive	Antoniewicz P et al. [100]
	SVM Predictive	Tao YK et al. [115]; Cho Y et al. [110]
	Table	Baktash A et al. [87]; Razali A et al. [88]; Zhi D et al. [89]; Malinowski M et al. [90]

Table 2. *Cont*.

Techniques		Researchers
Voltage	Model Predictive	Kwak S et al. [97,99]; Cortes P et al. [98]
	Vector Duty Cycle Control Predictive	Zhang Y et al. [111]; Fischer JR et al. [112]; Bouafia A et al. [113]; Restrepo JA et al. [114]
	SVM Predictive	Hu J et al. [103,106]; Choi D et al. [104]; Aurtenechea S et al. [105]; Song Z et al. [107]; Vazquez S et al. [108]; Zhang Y et al. [109]
	Model Adaptive	Portillo R et al. [119]; Vazquez S et al. [120]
	Vector Duty Cycle Control Table-based	Zhang Y et al. [123]
	Output Regulation Subspaces Table-based	Escobar G et al. [122]
	Sliding Mode	Hu J et al. [116]
	Fuzzy Logic	Bouafia A et al. [117,118]

3.2. Application of Direct Power Control on the PMSG Wind Power System

Grid Side Converter

From the block diagram in Figure 7, the grid-side static converter is a three-phase inverter connected to the grid through a filter. The DC voltage at the terminals of the capacitor and the current i_{ond} represent the electrical input quantities of the inverter. At the output, the inverter generates three-phase currents denoted $i_{f,abc}$ and alternating three-phase voltages denoted $V_{f,abc}$. The output of the inverter is connected to the grid through a filter of resistor R_f and inductance L_f. On the other side, the grid voltages will be represented by $V_{g,abc}$. Terms $(S_{o,abc}; S_{o,a'b'c'})$ represent the switching functions of the arms of the three-phase inverter.
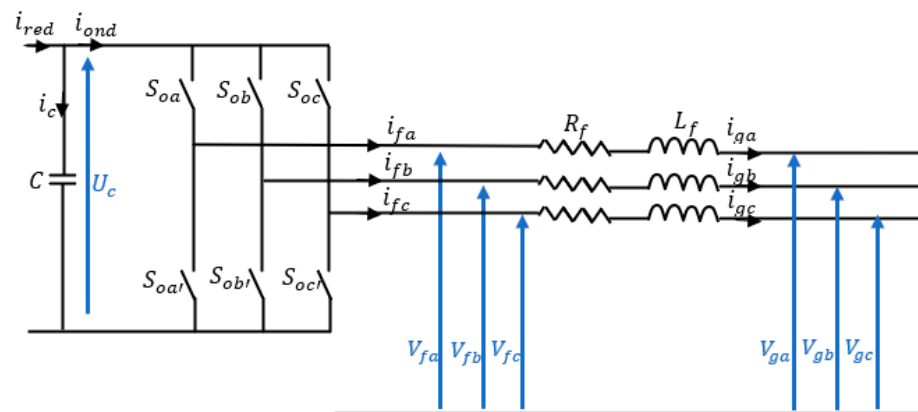
Figure 7. Grid-side converter.

In order to model the electronic switches, we consider that IGBT transistors form them antiparallel to diodes. As a hypothesis, they are all considered ideal, meaning they have an instantaneous response to control signals. The closed position is equivalent to zero resistance, and the open position is equal to infinite resistance.

The mathematical model of the switching functions of the arms of the converters (inverter) is defined by:

$$S_i = \begin{cases} 1, \rightarrow S_{i'} = 0 \\ 0, \rightarrow S_{i'} = 1 \end{cases} \tag{24}$$

With: i = oa, ob, oc.

The capacitor "C" is crossed by a current "i_C" which will be defined by:

$$i_C = i_{red} - i_{ond} = C \cdot \frac{dU_C}{dt} \tag{25}$$

Moreover,

$$i_{red} = S_{ra}i_{sa} + S_{rb}i_{sb} + S_{rc}i_{sc} \tag{26}$$

The expression of the voltage U_c will then be:

$$C \cdot \frac{dU_C}{dt} = S_{ra}i_{sa} + S_{rb}i_{sb} + S_{rc}i_{sc} - i_{ond} \tag{27}$$

The system of equations will represent the output voltages:

$$\begin{cases} V_{fa} = \frac{2S_{oa} - S_{ob} - S_{oc}}{3} U_C \\ V_{fb} = \frac{2S_{ob} - S_{oa} - S_{oc}}{3} U_C \\ V_{fc} = \frac{2S_{oc} - S_{ob} - S_{oa}}{3} U_C \end{cases} \tag{28}$$

The current i_{ond} will be defined by:

$$i_{ond} = S_{oa}i_{fa} + S_{ob}i_{fb} + S_{oc}i_{fc} \tag{29}$$

The three-phase output currents of the inverter $i_{f,abc}$ are determined by the system of equations:

$$\begin{cases} R_f i_{fa} + L_f \frac{di_{fa}}{dt} = V_{fa} - V_{ga} = \frac{2S_{oa} - S_{ob} - S_{oc}}{3} U_C - V_{ga} \\ R_f i_{fb} + L_f \frac{di_{fb}}{dt} = V_{fb} - V_{gb} = \frac{2S_{ob} - S_{oa} - S_{oc}}{3} U_C - V_{gb} \\ R_f i_{fc} + L_f \frac{di_{fc}}{dt} = V_{fc} - V_{gc} = \frac{2S_{oc} - S_{ob} - S_{oa}}{3} U_C - V_{gc} \end{cases} \tag{30}$$

The DPC control algorithm is generally based on the voltages represented in the reference plane (α-β). The space vector converter voltage is described in terms of switching states and voltage U_C by:

$$V_{\alpha\beta} = \sqrt{\frac{2}{3}} \left(S_{oa} + S_{ob}e^{j\left(\frac{2\pi}{3}\right)} + S_{oc}e^{j\left(\frac{4\pi}{3}\right)} \right) U_C \tag{31}$$

According to this last equation (Equation (31)), the spatial voltage vectors V_k generated by a two-level inverter can be represented in Table 3, where two vectors of the eight possible combinations are inactive and equal to zero.

The relation which links the voltage vector $V_{g,\alpha\beta}$ and the current transit vector to the grid $i_{g,\alpha\beta}$ can be represented by:

$$V_{g,\alpha\beta} = L_f \frac{di_{f,\alpha\beta}}{dt} + R_f i_{f,\alpha\beta} + V_{\alpha\beta} \tag{32}$$

a. **Switching table-based direct power control**

The principle of table-based DPC control needs the output variables of the hysteresis comparators and the voltage sector θ_{R-i} as shown in Figure 8.
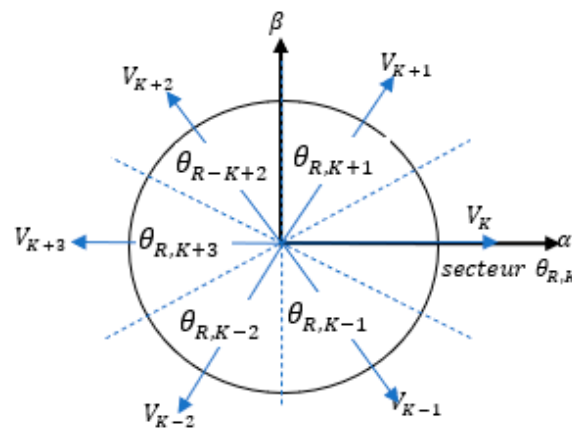
Figure 8. 6-sector tension plane in the frame (α-β).

The position of the voltage vector is obtained by using the following formula:

$$\angle\theta_R = \tan^{-1}\left(\frac{V_{g\beta}}{V_{g\alpha}}\right) \tag{33}$$

The role of hysteresis comparators is decisive in arriving at active and reactive power control signals. The switching table is built according to several criteria: the number of sectors chosen, the dynamic performance, and the type of hysteresis controller used (two or three levels).

Usually, the vector plane is divided into 6 sectors. They are defined by:

$$(2n-3)\frac{\pi}{6} \le \theta_{Rn} < (2n-1)\frac{\pi}{6} \tag{34}$$

With: $n = 1, 2, \ldots, 6$.

Table 3. Voltage vectors and switching states.

S_{oa}, S_{ob}, S_{oc}	V_K	v_α	v_β
1, 0, 0	$V_1 = \sqrt{\frac{2}{3}}U_C e^{j0}$	$\sqrt{\frac{2}{3}}U_C$	0
1, 1, 0	$V_2 = \sqrt{\frac{2}{3}}U_C e^{j\frac{\pi}{3}}$	$\sqrt{\frac{1}{6}}U_C$	$\frac{1}{\sqrt{2}}U_C$
0, 1, 0	$V_3 = \sqrt{\frac{2}{3}}U_C e^{j\frac{2\pi}{3}}$	$\frac{-1}{\sqrt{6}}U_C$	$\frac{1}{\sqrt{2}}U_C$
0, 1, 1	$V_4 = \sqrt{\frac{2}{3}}U_C e^{j\pi}$	$-\sqrt{\frac{2}{3}}U_C$	0
0, 0, 1	$V_5 = \sqrt{\frac{2}{3}}U_C e^{j\frac{4\pi}{3}}$	$\frac{-1}{\sqrt{6}}U_C$	$\frac{-1}{\sqrt{2}}U_C$
1, 0, 1	$V_6 = \sqrt{\frac{2}{3}}U_C e^{j\frac{5\pi}{3}}$	$\sqrt{\frac{1}{6}}U_C$	$\frac{-1}{\sqrt{2}}U_C$
0, 0, 0	$V_0 = 0$	0	0
1, 1, 1	$V_7 = 0$	0	0

Table 4 summarizes the states of evolution of the active and reactive powers according to the vectors selection with six sectors.

Table 4. Inverter switching table for 6 sectors.

Active Power: d_{P_g}	Reactive Power: d_{Q_g}	θ_{R1} $[-30°,30°]$	θ_{R2} $[30°,90°]$	θ_{R3} $[90°,150°]$	θ_{R4} $[150°,210°]$	θ_{R5} $[210°,270°]$	θ_{R6} $[270°,360°]$
1	0	$V_{6(1,0,1)}$	$V_{1(1,0,0)}$	$V_{2(1,1,0)}$	$V_{3(0,1,0)}$	$V_{4(0,1,1)}$	$V_{5(0,0,1)}$
1	1	$V_{0(0,0,0)}$	$V_{7(1,1,1)}$	$V_{0(0,0,0)}$	$V_{7(1,1,1)}$	$V_{0(0,0,0)}$	$V_{7(1,1,1)}$
0	0	$V_{6(1,0,1)}$	$V_{1(1,0,0)}$	$V_{2(1,1,0)}$	$V_{3(0,1,0)}$	$V_{4(0,1,1)}$	$V_{5(0,0,1)}$
0	1	$V_{1(1,0,0)}$	$V_{2(1,1,0)}$	$V_{3(0,1,0)}$	$V_{4(0,1,1)}$	$V_{5(0,0,1)}$	$V_{6(1,0,1)}$

b.   Dynamics performance:

Voltage vectors affect the instantaneous active and reactive power dynamics. Therefore, the expressions of the power dynamics can be formulated by:

$$\frac{d_{P_g}}{dt} = \frac{1}{L_f}\left(V_{g\alpha}^2 + V_{g\beta}^2\right) - \frac{1}{L_f}\left(V_{g\alpha}V_{c\alpha} + V_{g\beta}V_{c\beta}\right) \tag{35}$$

$$\frac{d_{Q_g}}{dt} = \frac{1}{L_f}\left(V_{g\alpha}V_{c\beta} - V_{g\beta}V_{c\alpha}\right) \tag{36}$$

With:

$V_{c\alpha}$ and $V_{c\beta}$: represent the Concordia components of the inverter output voltage.

The combinations of each inverter voltage vector used for the instantaneous power variation are summarized in Table 5 [129]. In this table, the sign (+) means a minor variation, while the sign (++) means a significant variation. As can be seen from the table, we have the following combinations:

- An increase in reactive power is obtained by applying the voltage vectors V_K, V_{K+1}, V_{K+2}.
- A decrease in reactive power is obtained by applying the voltage vectors V_{K-1}, V_{K-2}, V_{K+3}.
- An increase in active power is obtained by applying the voltage vectors V_{K+1}, V_{K+2}, V_{K+3}, V_{K-2}, V_0, V_7.
- A decrease in reactive power is obtained by applying the voltage vectors V_K, V_{K-1}.

Table 5. Instantaneous variations of active and reactive powers due to applied voltage vectors.

	V_{K-2}	V_{K-1}	V_K	V_{K+1}	V_{K+2}	V_{K+3}	V_0	V_7
Q_g	$--$	$-$	$++$	$+$	$+$	$-$	$+$	$-$
P_g	$+$	$-$	$-$	$+$	$++$	$++$	$+$	$+$

Figure 9 illustrates the general structure of DPC of the PMSG-wind energy conversion system.
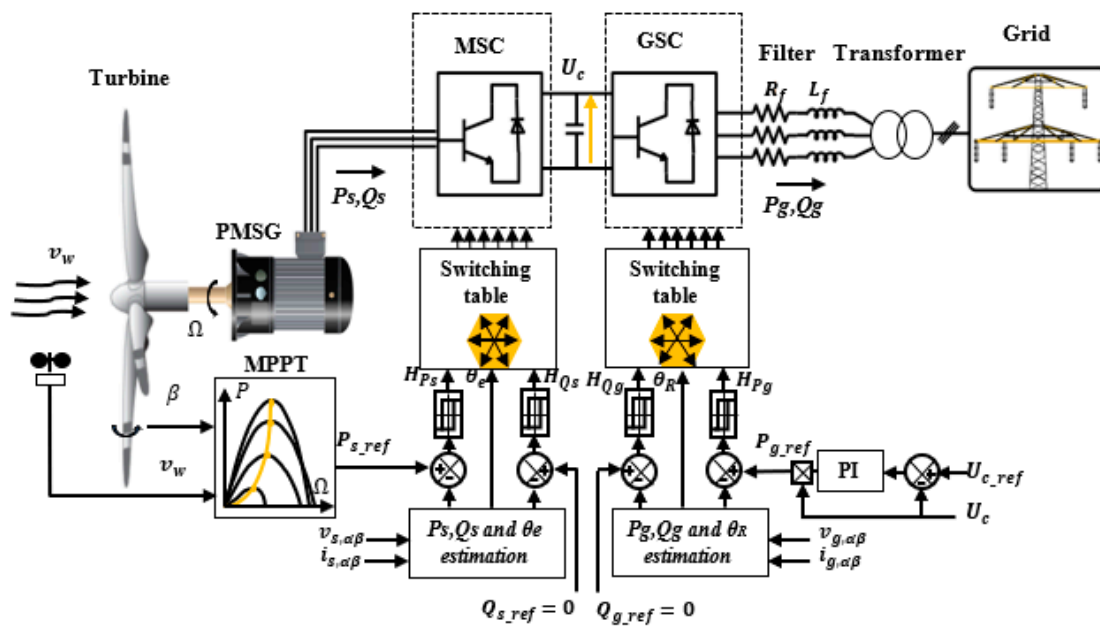
Figure 9. Synoptic schema of DPC applied to the PMSG-wind energy conversion system.

The design of switching tables employed in DPC control algorithms is a hot topic for researchers. Most of the research works summarized in Table 6 use simplifying assumptions for their work, and in most cases, they have assumed that the network voltage is ideal, which is not always the case in practice. Table 6 summarizes a performance comparison between different employed table-based DPC techniques, namely, VF-DPC, V-DPC and RV-DPC.

Table 6. Comparison between different employed table-based DPC techniques.

Reference Paper	Table-Based DPC	Active Power Variation		Voltage Sensors	Current THD	Active Power Ripple	Response Time	Switching Loss
		$d_{P_g}=1$ $d_{Q_g}=0$	$d_{P_g}=1$ $d_{Q_g}=1$					
[94]	RV-DPC	Little	Zero	Include	Low	Minimal	Slow	Small
[90]	VF-DPC	Medium	Zero	Exclude	High	Maximal	Slow	Small
[88]		Little	Very little	Include	Low	Minimal	Slow	Small
[130]		Little	Zero	Exclude	Low	Minimal	Slow	Small
[131]		Medium	Zero	Exclude	High	Maximal	Slow	Small
[96]	V-DPC	Medium	Zero	Exclude	High	Maximal	Slow	Small
[95]		Little	Big	Exclude	Medium	Medium	Medium	Medium
[132]		Very little	Big	Exclude	Medium	Medium	Fast	Large
[133]		Little	Medium	Include	Low	Minimal	Slow	Small
[134]		Very little	Very little	Include	Medium	Medium	Medium	Medium
[135]		Big	Very little	Include	Medium	Medium	Fast	Large
[136]		Little	Very little	Include	Low	Minimal	Slow	Small
[137]		Little	Zero	Include	Low	Minimal	Slow	Small
[138]		Little	Big	Include	Medium	Medium	Medium	Medium
[139]		Little	Big	Include	Medium	Medium	Medium	Medium

4. Backstepping Control

4.1. Review of Backstepping Control

In recent years, many researchers have been interested in recursive techniques in design controllers for nonlinear systems. Backstepping is a systematic method for nonlinear control design; it can be applied to a general class of systems. Its name refers to the recursive nature of the procedure conception [140]. The backstepping controller's principle converts a complex system into cascaded first-order subsystems. First, a small subsystem is considered for which a virtual control law is designed. Then the design is extended over several stages until the final control law for the overall system is constructed. Hence, nonlinear systems become linear despite the uncertainties. During the conception, a Lyapunov function of the controlled system is successfully constructed, increasing the system stability [141–144]. There are two types of backstepping techniques. The first type is called the non-adaptive backstepping control. This technique is used when the parameters of the studied system are known. The second type is called adaptive backstepping control. The adaptation law is used to estimate the various unknown parameters so that they converge towards their own values without affecting the system's overall stability. Hence, the system becomes insensitive to parametric variations [145].

The main drawback of the classical BSC is a phenomenon called "explosion of terms". This phenomenon occurs when virtual inputs are differentiated several times. As a result, the complexity of the controller increases, especially for higher-order systems, which makes the practical implementation of the control more difficult [145]. Many solutions have been introduced in the literature to improve the classical BSC.

The following figure shows the improved control structures of SMC that have been proposed to improve the conventional BSC (Figure 10).
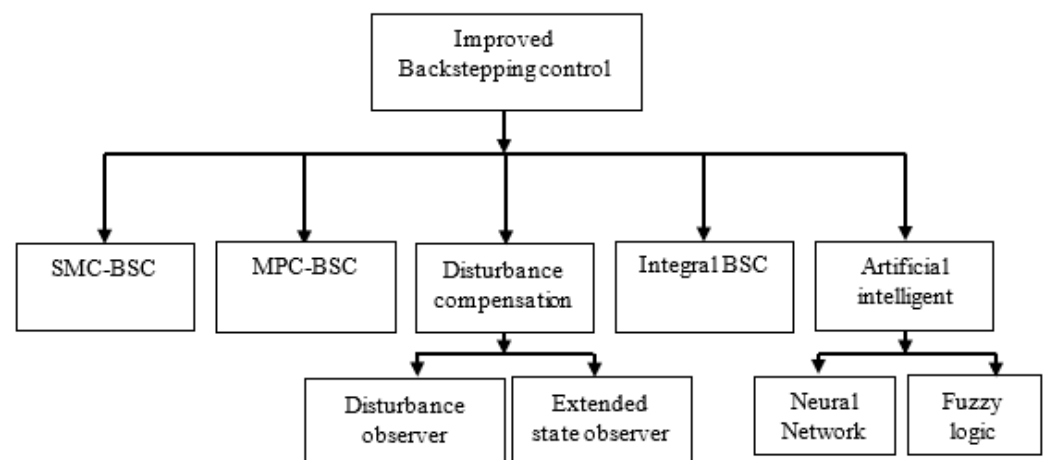

Figure 10. Summary of BSC enhancement techniques.

Many adaptations have been made to the backstepping controller design to solve the abovementioned problem. In [145] authors proposed a nonlinear adaptive filter with a positive time-varying integral function to avoid the issue of the explosion of complexity caused by the recursive procedure. This filter may effectively eliminate the effect raised by the boundary layer error at each step. In [146] authors proposed a specific control parameter that is based on the fuzzy rules. This control uses only one fuzzy system in each subsystem to approximate the unknown control gain and the unknown nonlinear function, as well as the differential of the former subsystem's virtual control. Contrary to the previous suggestion, Song et al. [147] chose to use both neuro and fuzzy systems in each subsystem. Meanwhile, Guangming et al. [148] chose to synthesize the fuzzy backstepping sliding mode tracking control method with the fractional CF technique to overcome such a shortcoming. In [149], the authors tried to combine the benefits of the disturbance observer with SMC under the framework of backstepping. Jiuwu et al. [150] combined another type

of observers controller, extended state observer (ESO), with backstepping controller. This observer was used to estimate both unmeasured states and output disturbances online. In the same context, Yeonsoo et al. [151] employed the model predictive technique (MPC) in the backstepping controller to design the first step's virtual input.

On the other hand, some authors tried to improve classical backstepping in terms of robustness, stability, and reference tracking. In this context, Nizami et al. [152] proposed a new control mechanism based on a Chebyshev neural network embedded in an adaptive backstepping framework. In [153] authors suggested a robust technique that adaptively estimates the nonlinear parameter uncertainties. This technique is based on a recurrent radial basis function neural network uncertainty online observer to solve both parameter variations and inevitable approximation, while Bossoufi et al. [154] used the rooted tree optimization (RTO) algorithm. The performance of this technique was confirmed through a test bench based on a dSPACE card. Integral backstepping is a further enhancement of the classical backstepping approach. In this technique, an integral action is added to the error terms to increase the controlled system's precision and stability [155–158].

Table 7 summarizes the different techniques used for the BSC control found in the literature.

Table 7. Various techniques used for BSC control.

	Techniques	Researchers
Backstepping	Filter	Liu Y-H [145]; Nizami et al. [152]
	Artificial intelligence	Shen X et al. [142]; Min W [146]; Song S [147]; Belkhier Y [159]
	Integral BSC	Makhad M et al. [155]; Loucif, M et al. [157]; Eluri N.V.D.V. Prasad et al. [158]
	Disturbance observer	Wang F et al. [149];
	Extended state observer	Jiuwu et al. [150]
	MPC-BSC	Yeonsoo K et al. [151]
	SMC-BSC	Rajendran, S et al. [160]

4.2. Application of Backstepping Control on the PMSG Wind Power System

According to backstepping control principles and based on the system equations presented in the Appendix A, the backstepping control design can be determined by following successive steps, where each step provides references for the next design step [161–164].

4.2.1. Machine Side Control

Step 1: Mechanical speed controller design:
The following expression can define the tracking error of speed:

$$e_\Omega = \Omega_{ref} - \Omega \tag{37}$$

Its derivate is given as:

$$\dot{e}_\Omega = \dot{\Omega}_{ref} - \dot{\Omega} = \dot{\Omega}_{ref} - \frac{1}{J_{tot}}\left[T_{turb} - \frac{3p}{2}\left(\left(L_d - L_q\right)i_{sd}\cdot i_{sq} + i_{sq}\Phi_f\right) - f_c\Omega\right] \tag{38}$$

To reduce the speed tracking error, the current components are identified as virtual control elements and the Lyapunov function is chosen as follows:

$$V_1 = \frac{1}{2}e_\Omega{}^2 \tag{39}$$

The Lyapunov function derivative is therefore:

$$\begin{aligned}
\dot{V_1} &= e_\Omega \cdot \dot{e_\Omega} \\
&= -K_\Omega e_\Omega{}^2 + \frac{e_\Omega}{J_{tot}}\left(-T_{turb} + f_c\Omega + K_\Omega \cdot J_{tot} \cdot e_\Omega + \frac{3p}{2}i_{sq}\Phi_f\right) + \frac{3}{2 \cdot J_{tot}}p\left(L_d - L_q\right)i_{sd} \cdot i_{sq} \cdot e_\Omega
\end{aligned} \tag{40}$$

To maintain the first subsystem's stability, the Lyapunov function derivative $\dot{V_1}$ must be negative. Therefore, both i_{sd} and i_{sq} are chosen as follows:

$$\begin{cases} i_{sd\_ref} = 0 \\ i_{sq\_ref} = \frac{2}{3 \cdot p \cdot \Phi_f}\left(T_{turb} - f_c\Omega - K_\Omega \cdot J_{tot} \cdot e_\Omega\right) \end{cases} \tag{41}$$

i_{sd_ref} and i_{sq_ref} will be considered as virtual references for the second step.

Replacing the i_{sd_ref}, i_{sq_ref} and $\dot{\Omega}_{ref} = 0$ with their values in Equation (40) gives:

$$\dot{V_1} = -K_\Omega \cdot e_\Omega{}^2 \le 0 \tag{42}$$

Hence, the system described by Equation (42) becomes stable only if K_Ω is fixed to a positive value.

Step 2: Stator current controller design:

The machine-side converter control voltages v_{sd_ref} and v_{sq_ref} are designed in this step based on the virtual inputs of the system, which are the stator currents (i_{sd}, i_{sq}).

The following expressions define the stator current errors:

$$e_d = i_{sd\_ref} - i_{sd} \tag{43}$$

$$e_q = i_{sq\_ref} - i_{sq} \tag{44}$$

Based on Equations (43) and (44), the current error dynamic $\dot{e_d}$ and $\dot{e_q}$ can be presented as follows:

$$\dot{e_d} = \dot{i_{sd\_ref}} - \dot{i_{sd}} = 0 - \dot{i_{sd}} = \frac{1}{L_d}\left(R_s i_{sd} - p\Omega L_q i_{sq} - v_{sd}\right) \tag{45}$$

$$\dot{e_q} = \dot{i_{sq\_ref}} - \dot{i_{sq}} = \frac{2}{3 \cdot p \cdot \Phi_f}\left(-f_c\dot{\Omega} - K_\Omega \cdot J_{tot} \cdot \dot{e_\Omega}\right) + \frac{1}{L_q}\left(R_s i_{sq} + p \cdot L_d \cdot \Omega \cdot i_{sd} + p \cdot \Omega \cdot \Phi_f - v_{sq}\right) \tag{46}$$

With:

$$\dot{e_\Omega} = \frac{1}{J_{tot}}\left[-K_\Omega \cdot J_{tot} \cdot e_\Omega - \frac{3p}{2}\Phi_f \cdot e_q - \frac{3p}{2} \cdot \left(L_d - L_q\right)i_{sd} \cdot i_{sq}\right] \tag{47}$$

The $\dot{e_q}$ expression becomes:

$$\dot{e_q} = \frac{2}{3 \cdot p \cdot \Phi_f}\left(\left(K_\Omega \cdot J_{tot} - f_c\right)\left[T_{turb} - f_c \cdot \Omega - \frac{3p}{2} \cdot \left(L_d - L_q\right)i_{sd} \cdot i_{sq} + i_{sq}\Phi_f\right]\right) + \frac{1}{L_q}\left(R_s i_{sq} + p\Omega L_d i_{sd} + p\Omega\Phi_f - v_{sq}\right) \tag{48}$$

Another Lyapunov function must be adopted to determine the stator voltage references. This function takes into account both the rotation speed error and the stator currents errors:

$$V_2 = \frac{1}{2}\left(e_\Omega{}^2 + e_d{}^2 + e_q{}^2\right) \tag{49}$$

Using Equations (45), (47) and (48) the second Lyapunov function derivative becomes:

$$\dot{V_2} = \left(e_\Omega \dot{e_\Omega} + e_d \dot{e_d} + e_q \dot{e_q}\right) \tag{50}$$

$$\begin{aligned}
\dot{V_2} = -K_\Omega e_\Omega{}^2 - K_d e_d{}^2 \quad &-K_q e_q{}^2 + \frac{e_\Omega}{J_{tot}}\left(-\frac{3p}{2}\Phi_f e_q - \frac{3p}{2} \cdot \left(L_d - L_q\right)i_{sd} \cdot i_{sq}\right) + \frac{e_d}{L_d}\left(R_s i_{sd} - p\Omega L_q i_{sq} - v_{sd} + K_d L_d e_d\right) \\
&+ \frac{e_q}{L_q}\left[\frac{2L_q}{3 \cdot p \cdot J_{tot} \cdot \Phi_f}\left(\left(K_\Omega \cdot J_{tot} - f_c\right)\left[T_{turb} - f_c \cdot \Omega - \frac{3p}{2} \cdot \left(L_d - L_q\right)i_{sd} \cdot i_{sq} + i_{sq}\Phi_f\right]\right) + R_s i_{sq} + p\Omega L_d i_{sd} + p\Omega\Phi_f - v_{sq} + K_q L_q e_q\right]
\end{aligned} \tag{51}$$

According to the Lyapunov theorem, to ensure the stability of the subsystem, the derivative of V_1 must be negative. Therefore, K_d and K_q are fixed to a positive value while the following voltages are used as reference voltages:

$$\begin{cases} v_{sd\_ref} = R_s i_{sd} - p\Omega L_q i_{sq} + K_q L_q e_q - \frac{3p}{2 \cdot J_{tot}} L_d (L_d - L_q) i_{sd} \cdot e_\Omega \\ v_{sq\_ref} = \frac{2L_q}{3 \cdot p \cdot J_{tot} \cdot \Phi_f} \left((K_\Omega \cdot J_{tot} - f_c) \left[T_{turb} - f_c \cdot \Omega - \frac{3p}{2} \cdot (L_d - L_q) i_{sd} \cdot i_{sq} + i_{sq} \Phi_f \right] \right) \\ \quad + R_s i_{sq} + p\Omega L_d i_{sd} + p\Omega \Phi_f + K_q L_q e_q - \frac{3}{2 \cdot J_{tot}} p \cdot i_{sq} \Phi_f \cdot e_\Omega \end{cases} \quad (52)$$

4.2.2. Grid-Side Converter Control

The GSC is controlled for two main reasons: to keep the DC bus voltage constant and to ensure that energy is transferred efficiently to the distribution grid [161–164]. Based on the model of the GSC in the *d-q* referential presented in the Appendix A, the grid current and power can be represented as follows:

$$\begin{cases} \frac{di_{gd}}{dt} = \frac{v_{fd}}{L_f} - \frac{R_f}{L_f} \cdot i_{gd} + w_g \cdot i_{gq} - \frac{v_{gd}}{L_f} \\ \frac{di_{gq}}{dt} = \frac{v_{fq}}{L_f} - \frac{R_f}{L_f} \cdot i_{gq} - w_g \cdot i_{gd} - \frac{v_{gq}}{L_f} \\ P_g = \frac{3}{2} \left[v_{gd} \cdot i_{gd} + v_{gq} \cdot i_{gq} \right] \\ Q_g = \frac{3}{2} \left[v_{gq} \cdot i_{gd} - v_{gd} \cdot i_{gq} \right] \end{cases} \quad (53)$$

One can notice that power is directly proportional to the quadrature current component i_{gq} as well as the direct current component i_{gd}. The backstepping control can be designed based on the following steps.

The first step is to define the direct and quadrature grid current errors:

$$e_{gd} = i_{gd\_ref} - i_{gd} \quad (54)$$

$$e_{gq} = i_{gq\_ref} - i_{gq} \quad (55)$$

The derivative of the current tracking errors can be expressed as:

$$\dot{e}_{gd} = \dot{i}_{gd\_ref} - \dot{i}_{gd} \quad (56)$$

$$\dot{e}_{gq} = \dot{i}_{gq\_ref} - \dot{i}_{gq} \quad (57)$$

Introducing the Lyapunov function for current errors:

$$V_3 = \frac{1}{2} \left(e_{gd}^2 + e_{gq}^2 \right) \quad (58)$$

Taking the derivative of Equation (58) along the dynamics of the system:

$$\dot{V}_3 = \left(e_{gd} \dot{e}_{gd} + e_{gq} \dot{e}_{gq} \right) \quad (59)$$

Replacing $\dot{i}_{gd}$ and $\dot{i}_{gq}$ by their expression in Equation (59) gives:

$$\dot{V}_3 = -K_{gd} e_{gd}^2 - K_{gq} e_{gq}^2 + e_{gd} \left(\frac{v_{fd}}{L_f} - \frac{R_f}{L_f} i_{gd} + \omega_g i_{gq} - \frac{v_{gd}}{L_f} + K_{gd} e_{gd} \right) + e_{gd} \left(\frac{v_{fq}}{L_f} - \frac{R_f}{L_f} i_{gq} - \omega_g i_{gd} - \frac{v_{gq}}{L_f} + K_{gq} e_{gq} \right) \quad (60)$$

To make the Lyapunov derivative function negative and ensure system stability, both K_{gd} and K_{gq} were fixed to positive values, and the GSC reference voltages were chosen as follows:

$$\begin{cases} v_{fd-ref} = R_f i_{gd} - L_f \omega_g i_{gq} - L_f K_{gd} e_{gd} + v_{gd} \\ v_{fq-ref} = R_f i_{gq} + L_f \omega_g i_{gd} - L_f K_{gq} e_{gq} + v_{gq} \end{cases} \quad (61)$$

Additionally, the reference value of the direct current was fixed to zero to ensure an operation with unit power factor while the quadrature current reference was deduced from the bus regulator as shown Figure 11.

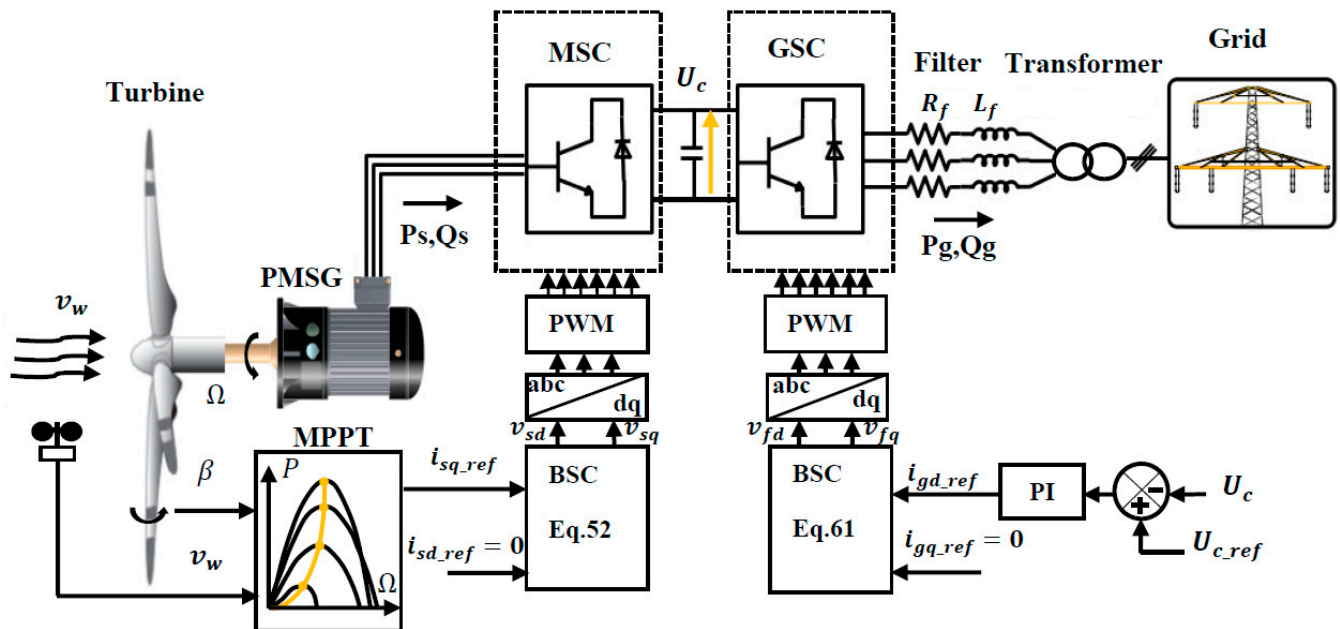Figure 11 illustrates the general structure of BSC of the PMSG-wind energy conversion system.

Figure 11. Synoptic schema of BSC applied to the PMSG-wind energy conversion system.

5. Model Predictive Control

5.1. Review of Model Predictive Control

In recent years, predictive control has emerged as a major control technique applicable to power converters and electric drives. Predictive control (MPC-model predictive control) uses the system model to predict the future behavior of the process for a specific control variable and then obtain an optimal action based on the predefined optimization criteria [132,165–168].

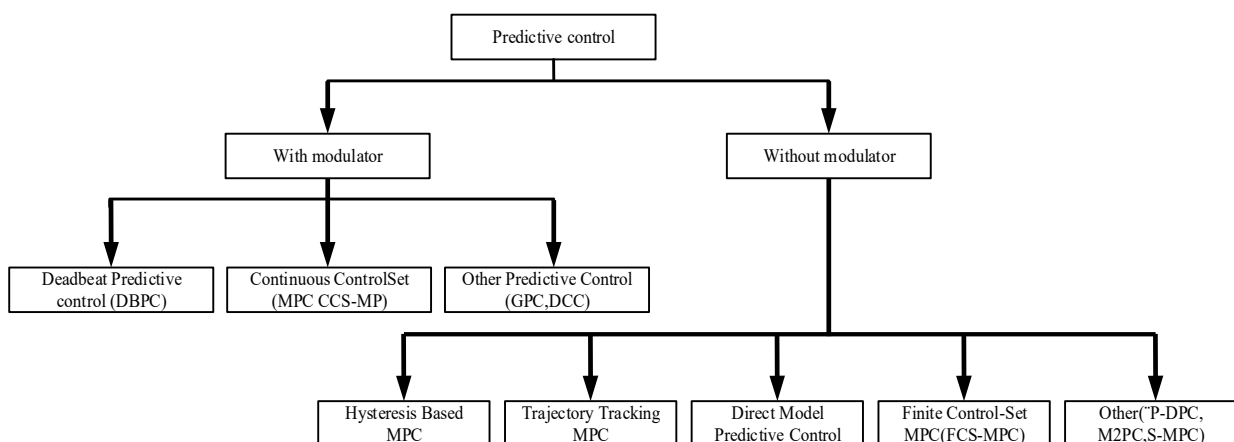A classification of the different predictive control strategies is shown in Figure 12 [168].

Figure 12. Classification of the different predictive control strategies.

Predictive deadbeat control calculates the control variable that cancels the error between the control variable and the reference input. This control technique has a fast dynamic

response, but its difficulty lies in the system parameters' variations and disturbances, which can cause deterioration in the obtained performances.

In addition, model predictive control (MPC) is recognized as a simple and powerful control strategy for controlling power converters because it is simple to apply in multi-variable systems, takes into account nonlinearities and constraints of the system to be controlled, and has a fast dynamic response [169,170]. This technique's operating principle is based on using a mathematical model to predict the system's future behavior, and then minimize the predefined cost function to achieve the specified control objectives.

MPC applied to power converters can be classified into two major categories: continuous control set MPC (CCS-MPC) and finite control set predictive control (FCS-MPC) [171]. In CCS-MPC, a modulator is required to generate the switching states, leading to a fixed switching frequency. However, the disadvantage of CCS-MPC is that the nonlinearities taken in the model lead to a complex optimization problem, which is difficult to solve online using a conventional hardware platform [171,172].

On the other hand, FCS-MPC predictive control relies on the discrete nature of the static converters due to the limitation of the number of their switching states. This advantage has the effect of reducing the calculation burden for both prediction and processing, as each converter has a limited number of switching states. The prediction procedure is also limited to these states [173–175]. Then, an optimization selects the optimal state (optimal voltage vector) to be applied to the charge. The main elements of this control technique are the mathematical model of the system and the predefined cost function [176–182].

Table 8 summarizes the different techniques used for the predictive control in the literature.

Table 8. Various techniques used for predictive control.

	Techniques	Researchers
With Modulator	Deadbeat predictive control (DBPC)	Nguyen, H et al. [183]; Bouderbala, M et al. [184]
	Continuous control-set (MPC-CCS-MP)	Balamurugan, A et al. [185,186]
	Other predictive control (GPC, DCC)	Shehata, E et al. [187]
Without Modulator	Hysteresis based (MPC)	Prince, M et al. [188]
	Trajectory tracking (MPC)	Cortes-Vega, D et al. [189]
	Direct model predictive control	Yip, S. Y. et al. [190]
	Other (P-DPC, M2PC, S-MPC)	Shehata, E. G. et al. [191]

5.2. Application of Model Predictive Control on the PMSG Wind Power System

In general, the implementation of FCS-MPC finite-state predictive control consists of four essential steps [192–195] as described below:

- Reference calculation: In this step, the reference control value $x^*(k)$ ($x \in$ voltage, current, power, torque, flux, etc.) is calculated depending on the application's nature.
- Prediction: this subsystem predicts the future values of the control variables $x^P(k+1)$ based on the DT model, the system parameters and the converter switching state combinations S(K).
- Extrapolation: the future value of the reference control variable $\hat{x}^*(k+1)$ is estimated in this step based on the current and past sample values $x^*(k), x^*(k-1)$.
- Cost Function Minimization: this function is used to minimize the error between the predicted and extrapolated references g = $\hat{x}^*(k+1) - x^P(k+1)$.

The following figure shows the general scheme of the FCS-MPC finite-state predictive control [196] (Figure 13).
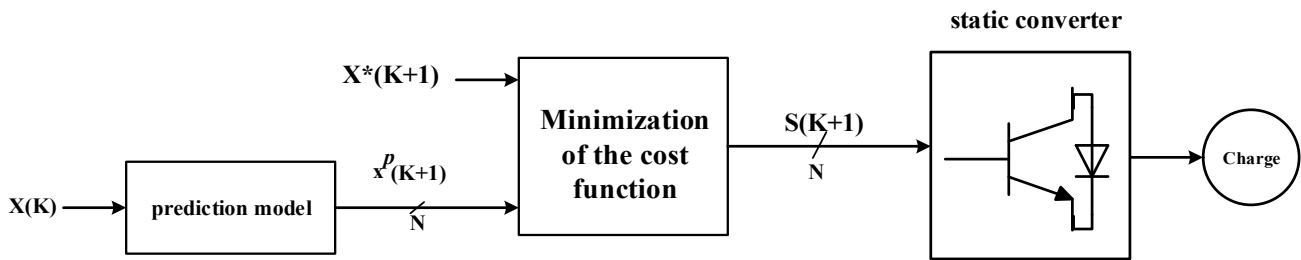

Figure 13. The general scheme of the FCS-MPC finite-state predictive control.

5.2.1. Machine-Side Control

As a first step for implementing the MPC control on the MSC side, a continuous-time dynamic model of PMSG stator currents must be given [197–200]. Considering the mathematical model of the PMSG in the *dq* reference frame shown in the Appendix A, the continuous-time model of PMSG can be represented in a simplified form as:

$$\frac{d}{dt}\begin{bmatrix} i_{sd}(t) \\ i_{sq}(t) \end{bmatrix} = A(t)\begin{bmatrix} i_{sd}(t) \\ i_{sq}(t) \end{bmatrix} + B\begin{bmatrix} v_{sd}(t) \\ v_{sq}(t) \end{bmatrix} + w(t) \tag{62}$$

where

$$A(t) = \begin{bmatrix} \frac{-R_s}{L_{sd}} & \frac{w_e(t)L_{sq}}{L_{sd}} \\ \frac{-w_e(t)L_{sd}}{L_{sq}} & \frac{-R_s}{L_{sq}} \end{bmatrix}; \ B = \begin{bmatrix} \frac{1}{L_{sd}} & 0 \\ 0 & \frac{1}{L_{sq}} \end{bmatrix}; \ w(t) = \begin{bmatrix} 0 \\ \frac{-w_e(t)\varphi_r}{L_{sq}} \end{bmatrix} \tag{63}$$

The next step in MPC implementation is to use a suitable discretization algorithm to convert the above continuous-time CT model into a discrete-time DT model. In this study a forward Euler approximation was used to simplify the analysis. This approach takes into account the future sample (*k* + 1) as well as the present sample (*k*), as seen below:

$$\left\{ \frac{dx(t)}{dt} \right\}_{t=kT_s} \approx \frac{x(kT_s + T_s) - x(T_s)}{T_s}, \ x \, \epsilon \, \{i_{sd}, i_{sq}\} \tag{64}$$

This later can be simplified as:

$$x(k+1) \approx x(k) + T_s\left\{ \frac{dx(t)}{dt} \right\}_{t=k} \tag{65}$$

After carrying out the required discretization, the discrete time DT model of the PMSG can be derived from Equation (62) as:

$$\begin{bmatrix} i_{sd}(k+1) \\ i_{sq}(k+1) \end{bmatrix} = \phi(k)\begin{bmatrix} i_{sd}(k) \\ i_{sq}(k) \end{bmatrix} + \Gamma_b\begin{bmatrix} v_{sd}(k) \\ v_{sq}(k) \end{bmatrix} + \Gamma_w(k) \tag{66}$$

With,

$$\begin{cases} \phi(k) \approx [I + A(k)T_s] \approx \begin{bmatrix} 1 - \frac{R_s T_s}{L_{sd}} & \frac{w_e(k)L_{sq}T_s}{L_{sd}} \\ -\frac{w_e(k)L_{ds}T_s}{L_{sq}} & 1 - \frac{R_s T_s}{L_{sq}} \end{bmatrix} \\ \Gamma_b \approx BT_s \approx \begin{bmatrix} \frac{T_s}{L_{sd}} & 0 \\ 0 & \frac{T_s}{L_{sq}} \end{bmatrix} \\ \Gamma_w(k) \approx w(k)T_s \approx \begin{bmatrix} 0 \\ -\frac{w_e(k)\varphi_r T_s}{L_{sq}} \end{bmatrix} \end{cases} \tag{67}$$

Considering the DT model of the PMSG machine given by Equation (66), the future behavior of the PMSG currents is predicted by calculating the future value of the currents. Hence, the predictive *dq*-axes currents can be represented as follows:

$$\begin{bmatrix} i_{sd}^p(k+1) \\ i_{sq}^p(k+1) \end{bmatrix} = \phi(k) \begin{bmatrix} i_{sd}(k) \\ i_{sq}(k) \end{bmatrix} + \Gamma_b \begin{bmatrix} v_{sd}^p(k) \\ v_{sq}^p(k) \end{bmatrix} + \Gamma_w(k) \tag{68}$$

where superscript *p* denotes the predicted variable.

The predicted MSC voltages v_{ds} and v_{qs} are obtained in terms of switching states and DC-link voltage (u_C) by the following model:

$$\begin{bmatrix} v_{sd}^p(k) \\ v_{sq}^p(k) \end{bmatrix} = u_C(k) \begin{bmatrix} s_{sd}^p(k) \\ s_{sq}^p(k) \end{bmatrix} \tag{69}$$

$u_C(k)$ is the capacitor voltage; $s_{s,dq}^p(k)$ is the *dq* axis state switching. its expression is as follows:

$$\begin{bmatrix} s_{sd}^p(k) \\ s_{sq}^p(k) \end{bmatrix} = \begin{bmatrix} cos\theta_e(k) & sin\theta_e(k) \\ -sin\theta_e(k) & cos\theta_e(k) \end{bmatrix} \frac{2}{3} \begin{bmatrix} 1 & -\frac{1}{2} & -\frac{1}{2} \\ 0 & \frac{\sqrt{3}}{2} & -\frac{\sqrt{3}}{2} \end{bmatrix} \begin{bmatrix} s_{sa}^p(k) \\ s_{sb}^p(k) \\ s_{sc}^p(k) \end{bmatrix} \tag{70}$$

By substituting Equation (69) into Equation (68), the predicted stator currents model becomes:

$$\begin{bmatrix} i_{sd}^p(k+1) \\ i_{sq}^p(k+1) \end{bmatrix} = \phi(k) \begin{bmatrix} i_{sd}(k) \\ i_{sq}(k) \end{bmatrix} + \Gamma_b \left(u_c(k) \begin{bmatrix} s_{sd}^p(k) \\ s_{sq}^p(k) \end{bmatrix} \right) + \Gamma_w(k) \tag{71}$$

On the other hand, the current references at (*k*) sampling instant are extrapolated to (*k* + 1) sampling instant by using first-order Lagrange extrapolation [201–206].

$$\begin{cases} \hat{i}_{sd}^*(k+1) = 2i_{sd}^*(k) - i_{sd}^*(k-1) \\ \hat{i}_{sq}^*(k+1) = 2i_{sq}^*(k) - i_{sq}^*(k-1) \end{cases} \tag{72}$$

where, $\hat{i}_{s,dq}^*$ is the extrapolated reference currents while $i_{s,dq}^*$ is the generator reference currents. to achieve a unity power factor in all operating conditions, the direct current i_{sd}^* is fixed to zero, whereas the i_{sq}^* is obtained by the MPPT control.

Finally, to minimize the error between predicted and extrapolated references currents, a cost function is used:

$$g_{MSC}(k) = \left[\hat{i}_{sd}^*(k+1) - i_{sd}^p(k+1) \right]^2 + \left[\hat{i}_{sq}^*(k+1) - i_{sq}^p(k+1) \right]^2 \tag{73}$$

5.2.2. Grid-Side Control Scheme

The dynamic model of the *dq*-axis grid currents in the continuous-time domain is given by:

$$\frac{d}{dt} \begin{bmatrix} i_{gd}(t) \\ i_{gq}(t) \end{bmatrix} = C(t) \begin{bmatrix} i_{gd}(t) \\ i_{gq}(t) \end{bmatrix} + D \begin{bmatrix} v_{fd}(t) \\ v_{fq}(t) \end{bmatrix} - D \begin{bmatrix} v_{gd}(t) \\ v_{gq}(t) \end{bmatrix} \tag{74}$$

where

$$C(t) = \begin{bmatrix} \frac{-R_f}{L_f} & w_g \\ -w_g & \frac{-R_f}{L_f} \end{bmatrix}, \ D = \begin{bmatrix} \frac{1}{L_f} & 0 \\ 0 & \frac{1}{L_f} \end{bmatrix} \tag{75}$$

By following the same procedure that was used for determining the MSC predictive controller, the GSC cost function can be presented as follows:

$$g_{GSC}(k) = \left[\hat{i}_{gd}^*(k+1) - i_{gd}^p(k+1) \right]^2 + \left[\hat{i}_{gq}^*(k+1) - i_{gq}^p(k+1) \right]^2 \tag{76}$$

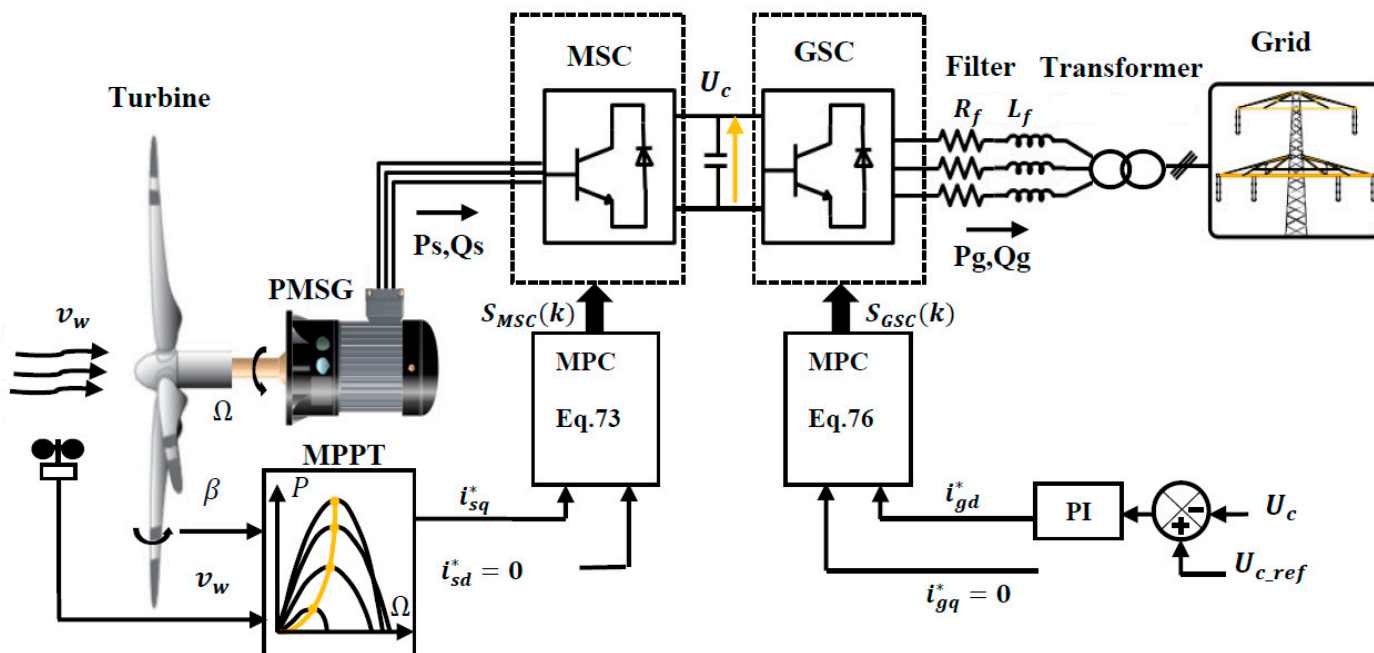Figure 14 illustrates the general structure of MPC of the PMSG-wind energy conversion system.

Figure 14. Synoptic schema of MPC applied to the PMSG-wind energy conversion system.

6. MPPT Control

According to Betz's law, turbines can not convert more than 16/27 (59.3%) of the kinetic energy into mechanical energy. This factor is known as Betz's coefficient and denoted $C_{pmax} = 0.593$. In fact, wind turbines achieve peak values for C_p in the range of 0.45 to 0.50, about 75–85% of the theoretically possible maximum. In this study, the WT produces maximum power when $C_{p\_max} = 0.48$. As shown in Figure 15, this maximum can be obtained when β and λ are equal to their optimum ($\lambda_{opt} = 0.8$, $\beta = 0°$). Therefore, in order to keep the power coefficient at maximum, the maximum power point tracking control strategy (MPPT) must be used [207–209].
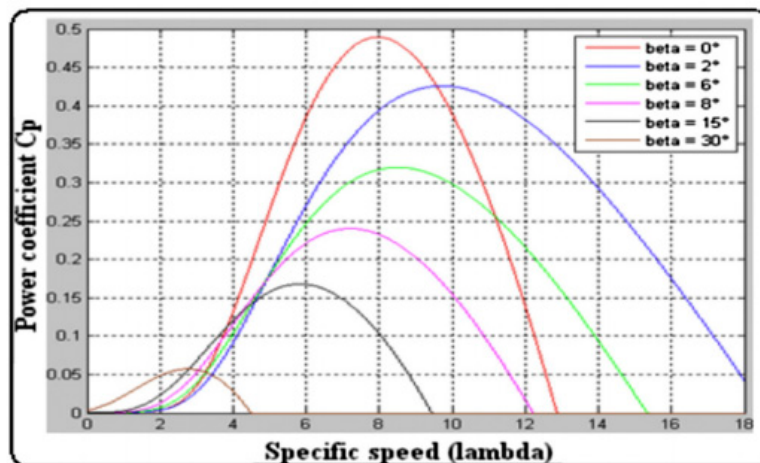
Figure 15. The relationship between the λ, β and C_p.

The MPPT algorithm extracts maximum power from available wind speed and turns the generator at its optimum speed [13]. As depicted in Figure 15, the WT produces the maximum power when the power coefficient C_p is at its maximum value C_{p_max} which depends on the λ_{opt} value. Therefore, the turbine's rotational speed must be constantly adjusted according to wind speed changes to the specific value that ensure the optimum tip speed ratio (TSR) λ_{opt}. In the literature, various MPPT algorithms for WT have been

proposed. A review of MPPT Algorithms for WECS is given in [14]. The TSR MPPT algorithm without speed measurement is widely used, and it is known for its simplicity, as well as its constant reliability and efficiency. As shown in Figure 16, this control strategy estimates the wind speed in real time and imposes a reference torque that allows the PMSG to rotate around its optimal speed.

Then, the estimated value of the wind speed is given by:

$$v_{est} = \frac{\Omega_{opt} \cdot R}{\lambda_{opt}} \tag{77}$$

The expression of the optimum power that can be extracted from the wind is as follows:

$$P_{turb\_opt} = \frac{1}{2} \cdot \varphi \cdot \pi \cdot R^2 \cdot C_{p\_max}(\lambda, \beta) \cdot v_w^3 \tag{78}$$

The expression of the reference electromagnetic torque becomes:

$$T_{turb\_opt} = \frac{P_{turb\_opt}}{\Omega} = \frac{1}{2} \cdot \varphi \cdot \pi \cdot R^2 \cdot C_{p\_max}(\lambda_{opt}, \beta) \cdot v_w^3 \cdot \frac{1}{\Omega} \tag{79}$$
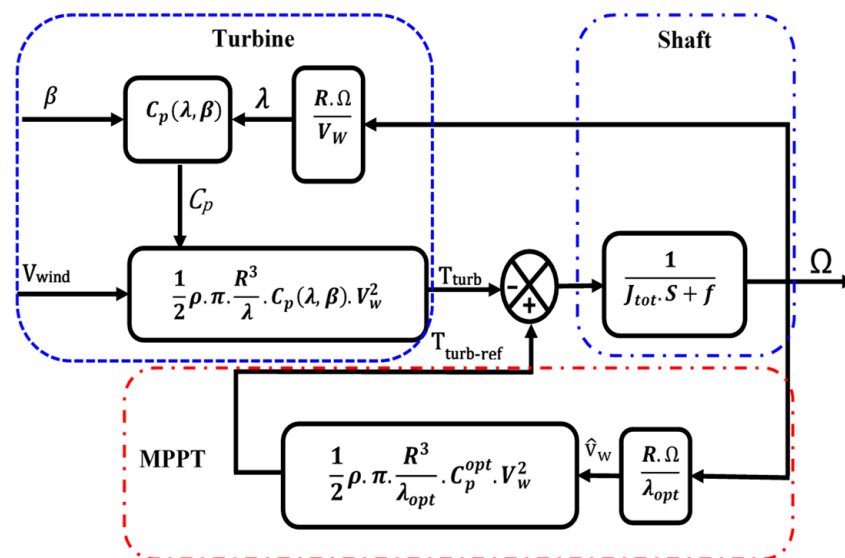

Figure 16. The MPPT strategy without speed measurement.

7. Results and Discussion

To show the effect of each classical control (SMC, DPC, BSC and MPC) on the dynamic and static performance of the WECS, a simulation test was performed under a variable wind profile in MATLAB/Simulink software. Figure 17a shows the wind profile that was used in this simulation.

The principal characteristics of this simulation are described as follows:

- The WECS parameters are mentioned in the Appendix A.
- The wind speed varies between 3.5 m/s and 8.5 m/s for 10 s.
- Grid frequency f = 50 Hz.
- To commute IGBT devices of two-level converters, pulse width modulation (PWM) was used in both SMC and BSC.
- A phase-locked loop (PLL) was used to synchronize the GSC to the grid in all control schemes except the DPC control scheme.

Figure 17b shows that the mechanical angular speed shape perfectly follows the set wind profile. The low value of the speed is due to a large number of poles in the machine. It can be seen from Figure 17c that the tip speed ratio λ (lambda) and the power coefficient

C_p are equal to their optimal value references, 8.1 and 0.48, respectively, despite wind speed changes. Furthermore, the mechanical power has a form similar to that of wind Figure 17d. These results ensure that the system operates around its optimum rotational speed, proving the MPPT control's efficiency.

Figure 18a,b shows the active and reactive powers of the different controls. Figure 18a illustrates the active power, which has the same shape as the wind profile. However, negative active power means that the machine is in generator mode. Figure 18b illustrates the reactive power, which has a zero value, ensuring a unit power factor.
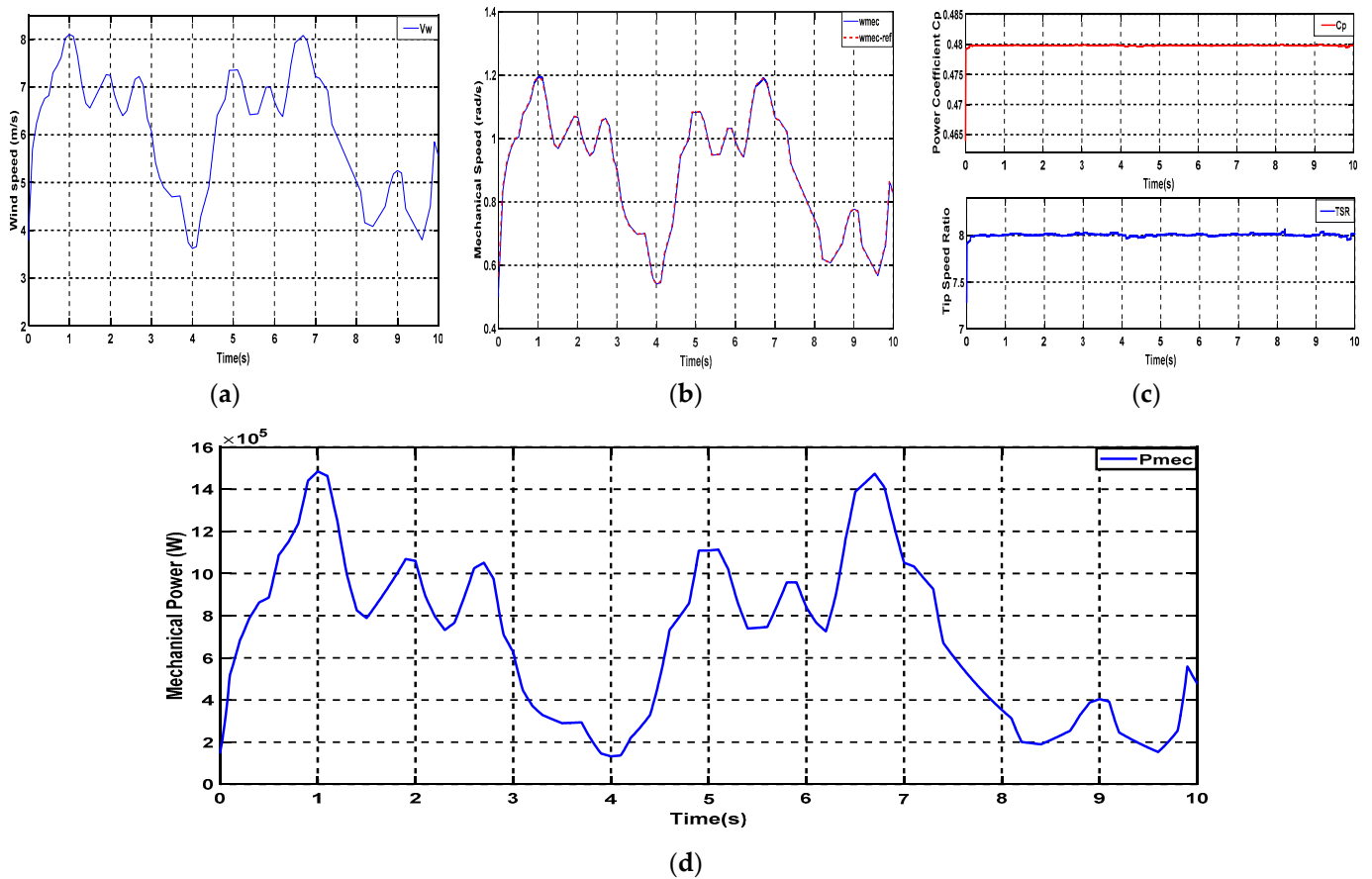

| (a) | (b) | (c) |

(d)

Figure 17. MPPT's performance: wind speed (m/s) (**a**), power coefficient C_p (λ, β) and tip speed ratio TSR (**b**), Mechanical Speed of the PMSG (**c**), Mechanical Power (**d**).

For all types of classical controls (SMC, DPC, BSC, and MPC) Figure 18a shows that the active power tracks its reference generated by the MPPT strategy precisely and without a coupling effect between the two axes, while the stator reactive power Qs (Figure 18b) remains close to zero to keep the unit power factor, thus optimizing the quality of the generated electrical energy. The notable difference that can be observed from these figures (Figure 18a,b) is that the PMSG wind turbine system performs better power oscillation and overshoot under MPC than the other controls. The chattering problem (high power oscillation) appears clearly in the shape of both $Ps_{(SMC)}$ and $Qs_{(SMC)}$ of the SMC. Almost the same problem can be observed in the curve of both the active and the reactive power ($Ps_{(DPC)}$, $Qs_{(DPC)}$) produced in the case of DPC control. And, as has been explained, these two phenomena are caused by the discontinuous function used in the SMC structure, and the hysteresis controllers used in the DPC design. However, the system's response time ($Tr_{(MPC)}$ = 0.05 s) of the predictive technique is a little slower than that of SMC, BSC, and DPC control which are characterized by a fast response time ($Tr_{(SMC)}$ = 0.025 s, $Tr_{(BSC)}$ = 0.03 s and $Tr_{(DPC)}$ = 0.048 s) (see zoom(1) Figure 18a). This delay is due to the excessive computational load of the MPC techniques.
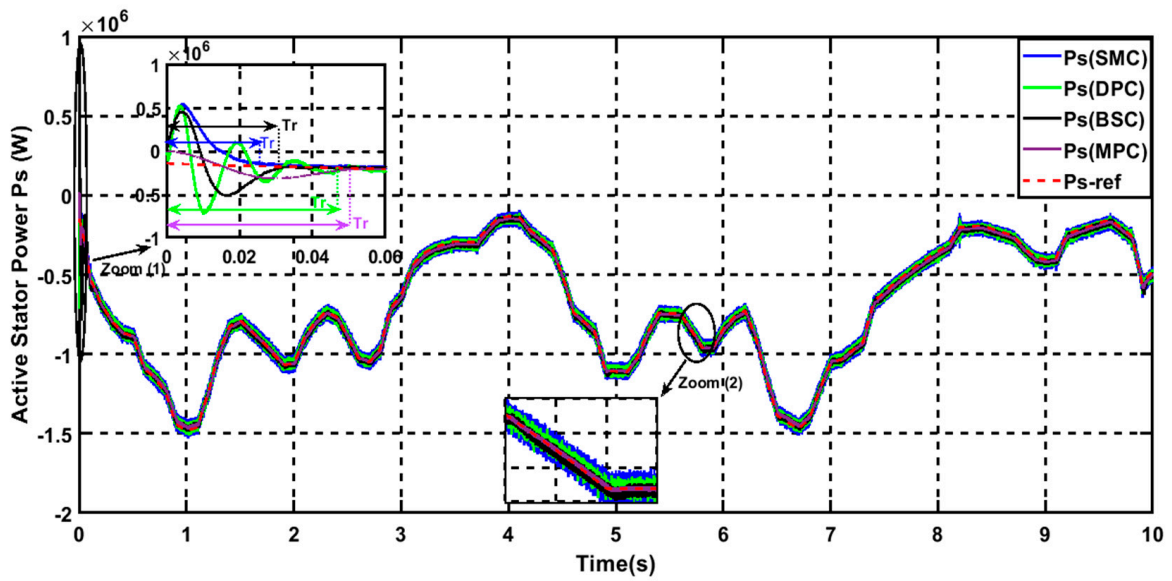
(**a**)
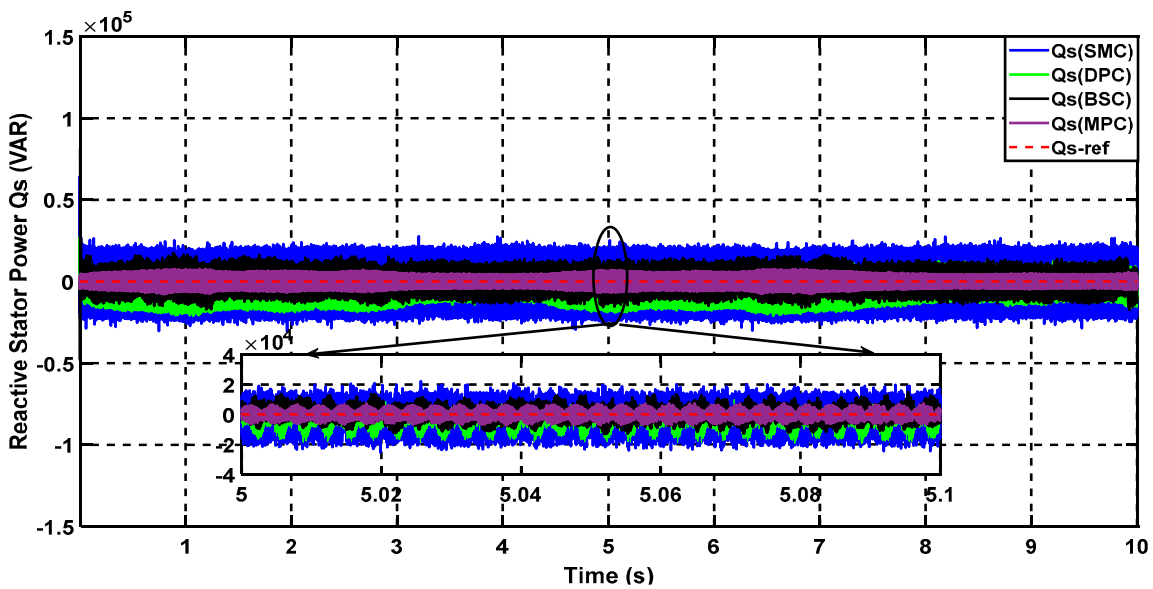
(**b**)

Figure 18. Active Stator power Ps (**a**), Reactive Stator Power Qs (**b**).

Figure 19 shows that the magnitude of the injected current varies according to the variation of the wind while the frequency remains constant at fs = 50 Hz for the four types of control. At the same time, the waveform of the injected current takes a better sinusoidal shape under MPC and BSC than that of both the SMC and DPC, where some unwanted distortion appears in their shapes (see zoom Figure 19a–d).
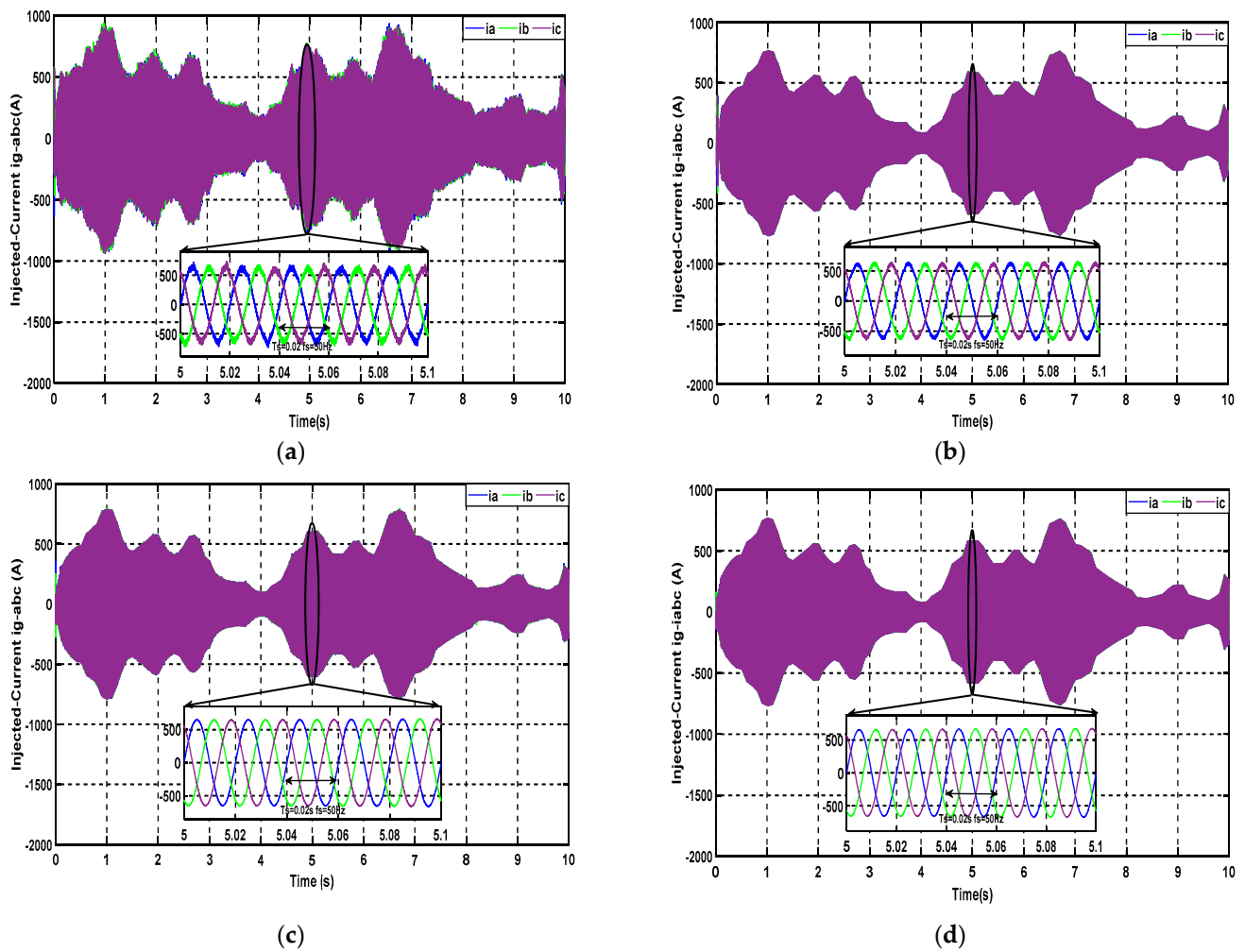
Figure 19. Injected current i$_{g\text{-}abc}$ by: SMC (**a**); DPC (**b**); BSC (**c**); MPC (**d**).

On the other hand, it is important to perform a harmonic analysis to check whether the injected current's THD rate meets the IEEE standard limit (TDH ≤ 5%). Figure 20 illustrates that the total harmonic distortion achieved by MPC and BSC (THD = 1.23%, THD = 1.91%) is considerably lower than that achieved by SMC and DPC (THD = 3.12%, THD = 2.77%).
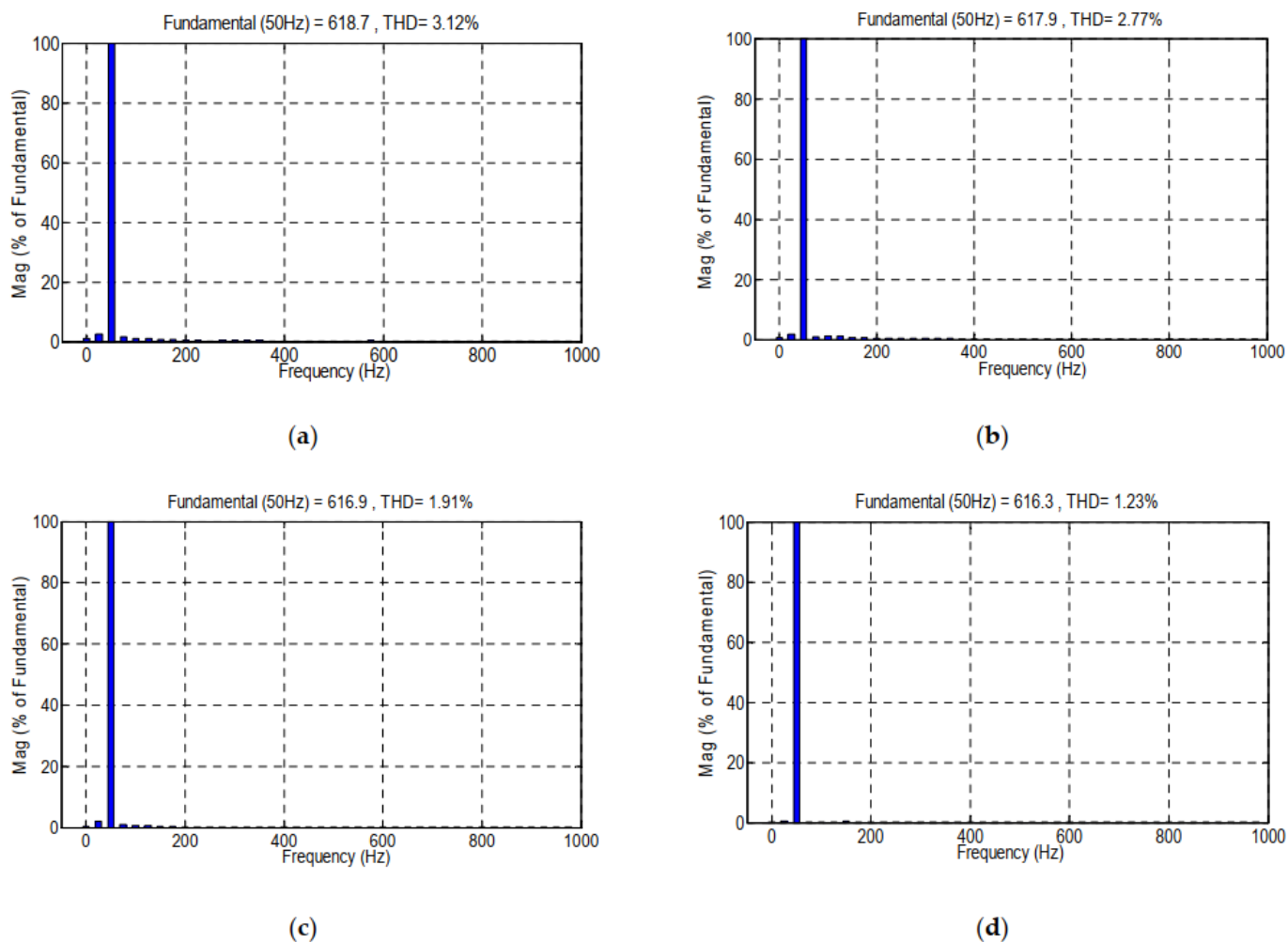
Figure 20. Spectrum analysis for the current injected ig-a by: SMC (**a**); DPC (**b**);BSC (**c**); MPC (**d**).

Considering the number of references cited in this work and the simulation results obtained, it was necessary to add a comparative analysis to this work to have a clear idea of the properties of each classical control and see its effect on the PMSG wind energy conversion system, as well as to see the level of agreement between the results obtained and what is written in the literature. The following table presents a comparative analysis between the four presented controls (Table 9):

Table 9. Comparison of the four reviewed controls.

| Controller | Simulations Results | | | | Literatures | |
	Tr (s)	ξ %	TDH %	Ease of Implementation	Remarkable Properties	Disadvantages
SMC	0.025	0.25	3.12	Simple	Strong performance in the face of uncertainties and disturbances. The system stability is guaranteed by using lyapunov function.	Requires the mathematical model of the system. Chattering problem.

Table 9. *Cont.*

	Simulations Results				Literatures	
Controller	Tr (s)	ξ %	TDH %	Ease of Implementation	Remarkable Properties	Disadvantages
DPC	0.048	0.32	2.77	Very Simple	Easier implementation and low complexity. PWM modulation blocks and internal regulating loops are not included.	Variable switching frequency. Large active and reactive power ripple bands.
BSC	0.030	0.17	1.91	Complicated	Uncertainties can be handled. Stability is ensured at every design step using the Lyapunov function.	Requires the mathematical model of the system. Complex design. Explosion of terms.
MPC	0.05	1.15	1.25	Simple	Easier implementation. Excellent performance under varying wind conditions. High flexibility.	Requires the mathematical model of the system. Excessive computational load.

8. Conclusions

This study presented an overview of the most popular control strategies that have been used to control the WECS based PMSG. The four controls, SMC, DPC, BSC, and MPC, were successfully reviewed and evaluated. First, the principles of each control were explained, followed by a discussion of the benefits and drawbacks of using these types of controls in the PMSG wind energy conversion system. Additionally, the various improvements applied to the classical controls proposed in the literature were highlighted. The MPPT control was also used in this work to get maximum power under a rapidly changing wind profile.

Furthermore, to check on the performance of each control, a simulation test of the four classical controls was performed in the MATLAB/Simulink software using a variable wind profile. Finally, a performance comparison between the four classical controls was presented. The simulation results show that the predictive control outperforms the conventional controls in terms of accuracy, simplicity, precision, reference point tracking, and the quality of the injected currents. Furthermore, it overcame the drawbacks of traditional control techniques, exemplified by the chattering phenomena of the SMC control, the high-power ripples caused by the DPC's hysteresis comparators, and the complexity of the backstepping. The simulation results were quite identical to what was published in the literature. Hence, this work can be considered a useful reference for novice researchers in the energy field to move ahead in the next decade.

Author Contributions: Conceptualization, B.M., H.E.A., H.S., N.Z.L.; methodology, B.M., H.E.A., H.S., N.Z.L.; software, B.M., H.E.A., H.S., N.Z.L.; validation, B.M., B.B.; formal analysis, B.M., H.E.A., H.S., N.Z.L.; investigation, B.M., H.E.A., H.S., N.Z.L.; resources, B.M., H.E.A., H.S., N.Z.L.; data curation, B.M., H.E.A., H.S., N.Z.L.; writing—original draft preparation, B.B., Y.E.M., S.M., M.B.; writing—review and editing, B.B., Y.E.M., S.M.; visualization, M.K., B.B., Y.E.M.; supervision, B.B., S.M.; project administration, B.B. All authors have read and agreed to the published version of the manuscript.

Funding: This research received no external funding.

Institutional Review Board Statement: Not applicable.

Informed Consent Statement: Not applicable.

Data Availability Statement: Not applicable.

Nomenclature

P_{turb}	$\Psi(d,q)$	d-q axis flux
v_w/P_{wind}	$\varnothing_f$	Generator flux
Ω	P_g	Active grid power
Ω_t	Q_g	Reactive grid power
T_{em}	U_C	DC-link voltage
T_{em_ref}	$V_g(d,q)$	d-q axis grid voltage
T_{turb}	$V_f(d,q)$	d-q axis filter voltage
$C_p(\lambda, \beta)$	$i_g(d,q)$	d-q axis grid current
λ	$i_f(d,q)$	d-q axis filter current
β	ω_g	Grid pulsation
ρ	R_f	Filter resistance
p	L_f	Filter inductance
S	WT	Wind turbine
R	WECS	Wind energy conversion system
Ω_e	MPPT	Maximum power point tracking
P_s	MPC	Model predictive control
Q_s	SMC	Sliding mode control
R_s	DPC	Direct power control
$L_s(d,q)$	BSC	Backstepping control
$V_s(d,q)$	Tr	Response time
$i_s(d,q)$	THD	Total harmonic distortion
f_c	PMSG	Permanent magnet synchronous generator
IGBT	PWM	Pulse width modulation

Appendix A

Table A1. PMSG and Wind Turbine parameters.

PMSG Parameters	Symbol	Values	Turbine Parameters	Symbol	Values
Power generator	P_n	1.5 MW	Radius of the turbine blade	R	55 m
Pole number	P	75			
Stator resistance	R_s	$6.25 \times 10^{-3}\ \Omega$	Turbine+ generator moment	J_{tot}	10,000 N.m
d axis inductance	L_{sd}	4.229×10^{-3} H	Specific density of air	ρ	1.22 kg/m^3
q axis inductance	L_{sq}	4.229×10^{-3} H	Tip-speed ratio	λ_{opt}	8
Generator flux	$\varnothing_f$	11.1464 Wb	Optimal power coefficient	C_{p_max}	0.426
Coefficient of friction	f_c	0.0142 N.m.s/rad			

Wind turbine modelling:

The kinetic power P_{wind} captured by the turbine and the mechanical power P_{turb} delivered to the PMSG are quantified by the two equations below.

$$P_{wind} = \frac{1}{2} \cdot \rho \cdot \pi \cdot R^2 \cdot v_w^3 \tag{A1}$$

$$P_{turb} = C_p(A, \beta) \cdot P_{wind} = \frac{1}{2} \cdot \rho \cdot \pi \cdot R^2 \cdot C_p(A, \beta) \cdot v_w^3 \tag{A2}$$

The mechanical torque T_{turb} is expressed as the quotient of the power transmitted to PMSG by its rotor mechanical speed, as follows.

$$T_{turb} = \frac{P_{turb}}{\Omega} = \frac{1}{2} \cdot \rho \cdot \pi \cdot R^2 \cdot C_p(\lambda, \beta) \cdot v_w^3 \cdot \frac{1}{\Omega} \tag{A3}$$

$C_p(A, \beta)$ represents the power coefficient of the wind turbine, which describes the capacity of the turbine to transform the wind kinetic power to mechanical power. Its

expression depends on the tip speed ratio λ and the pitch angle β [2–6], and it is often approximated by a specific non-linear function as follows:

$$C_p(\lambda, \beta) = 0.5176 \left(116 \left(\frac{1}{\lambda + 0.08 \cdot \beta} - \frac{0.035}{1 + \beta^3} \right) - 0.4\beta - 4 \right) e^{-21 \left(\frac{1}{\lambda + 0.08 \cdot \beta} - \frac{0.035}{1 + \beta^3} \right)} + 0.0068\lambda \tag{A4}$$

The tip-speed ratio λ is defined as the ratio between the blades' speed and the wind speed:

$$\lambda = \frac{\Omega \cdot R}{v_w} \tag{A5}$$

Permanent Magnet Synchronous Generator Model:

Based on the simplifying conditions, assumptions, and physical laws, the dynamic model of PMSG in the *d-q* reference frame can be described as follows:

- Stator Electric equations:

$$\begin{cases} v_{sd} = R_s \cdot i_{sd} + \frac{d\Psi_{sd}}{dt} - p \cdot \Omega \cdot \Psi_{sq} \\ v_{sq} = R_s \cdot i_{sq} + \frac{d\Psi_{sq}}{dt} + p \cdot \Omega \cdot \Psi_{sd} \end{cases} ; \ w_e = p \cdot \Omega \tag{A6}$$

- Stator Magnetic equations:

$$\begin{cases} \Psi_{sd} = L_{sd} \cdot i_{sd} + \varnothing_f \\ \Psi_{sq} = L_{sq} \cdot i_{sq} \end{cases} \tag{A7}$$

- Mechanical equations:

$$\begin{cases} J_{tot} \cdot \frac{d\Omega}{dt} = T_{mec} = T_{turb} - T_{em} - f_c \cdot \Omega \\ J_{tot} = J_{turb} + J_g \end{cases} \tag{A8}$$

The electromagnetic torque is then calculated as

$$T_{em} = \frac{3}{2} \cdot p \left[(L_{sd} - L_{sq}) i_{sd} \cdot i_{sq} + i_{sq} \cdot \varnothing_f \right] \tag{A9}$$

The active and reactive powers of the stator can be expressed as follows:

$$\begin{cases} P_s = \frac{3}{2} \left[v_{sd} \cdot i_{sd} + v_{sq} \cdot i_{sq} \right] \\ Q_s = \frac{3}{2} \left[v_{sq} \cdot i_{sd} - v_{sd} \cdot i_{sq} \right] \end{cases} \tag{A10}$$

Grid Model:

The grid voltages in the *d-q* referential can be presented as follows:

$$\begin{cases} v_{gd} = v_{fq} + R_f \cdot i_{gd} - L_f \frac{di_{gd}}{dt} + w_g \cdot L_f \cdot i_{gq} \\ v_{gq} = v_{fq} + R_f \cdot i_{gq} - L_f \frac{di_{gq}}{dt} - w_g \cdot L_f \cdot i_{gd} \end{cases} \tag{A11}$$

The active and reactive powers supplied into the grid are:

$$\begin{cases} P_g = \frac{3}{2} \left[v_{gd} \cdot i_{gd} + v_{gq} \cdot i_{gq} \right] \\ Q_g = \frac{3}{2} \left[v_{gq} \cdot i_{gd} - v_{gd} \cdot i_{gq} \right] \end{cases} \tag{A12}$$

References

1. IEA. *Key World Energy Statistics 2020*; IEA: Paris, France, 2020. Available online: https://www.iea.org/reports/key-world-energy-statistics-2020 (accessed on 15 May 2022).
2. Allouhi, A.; Kousksou, T.; Jamil, A.; Bruel, P.; Mourad, Y.; Zeraouli, Y. Solar driven cooling systems: An updated review. *Renew. Sustain. Energy Rev.* **2015**, *44*, 159–181. [CrossRef]

3. REN21. *Renewables 2015 Global Status Report (Paris: REN21 Secretariat)*; REN21: Paris, France, 2015; ISBN 978-3-9815934-6-4.
4. Kalogirou, S.A. Chapter 3—Solar Energy Collectors. In *Solar Energy Engineering*, 2nd ed.; Academic Press: Boston, MA, USA, 2014; pp. 125–220.
5. Cheng, M.; Zhu, Y. The state of the art of wind energy conversion systems and technologies: A review. *Energy Convers. Manag.* **2014**, *88*, 332–347. [CrossRef]
6. Boulouiha, H.M.; Allali, A.; Denai, M. Grid integration of wind energy systems: Control design, stability, and power quality issues. In *Clean Energy for Sustainable Development*; Elsevier: Amsterdam, The Netherlands, 2017; pp. 239–335.
7. Khare, V.; Nema, S.; Baredar, P. Solar–wind hybrid renewable energy system: A review. *Renew. Sustain. Energy Rev.* **2016**, *58*, 23–33. [CrossRef]
8. Bundi, J.M.; Ban, X.; Wekesa, D.W.; Ding, S. Pitch control of small H-type Darrieus vertical axis wind turbines using advanced gain scheduling techniques. *Renew. Energy* **2020**, *161*, 756–765. [CrossRef]
9. Zhao, Y.; Wei, C.; Zhang, Z.; Qiao, W. A review on position/speed sensorless control for permanent magnet synchronous machine-based wind energy conversion systems. *IEEE J. Emerg. Sel. Top. Power Electron.* **2013**, *1*, 203–216. [CrossRef]
10. Mourabit, Y.E.; Derouich, A.; Allouhi, A.; Ghzizal, A.E.; Ouanjli, N.E.; Zamzoumyes, O. Sustainable production of wind energy in the main Morocco's sites using permanent magnet synchronous generators. *Int. Trans. Electr. Energy Syst.* **2020**, *30*, e12390. [CrossRef]
11. Bossoufi, B.; Karim, M.; Lagrioui, A. *Contribution à la Commande de la Machine Synchrone à Aimant Permanent, Utilisation des Solutions Numériques FPGA*; Presses Académiques Francophones (PAF): Sarrebruck, Germany, 2015; p. 184.
12. Bossoufi, B. *Contrôle des Machines Electriques et Convertisseurs de Puissance*; Editions Universitaires Européennes: Sarrebruck, Germany, 2020.
13. Bekiroglu, E.; Yazar, M.D. MPPT Control of Grid Connected DFIG at Variable Wind Speed. *Energies* **2022**, *15*, 3146. [CrossRef]
14. Pande, J.; Nasikkar, P.; Kotecha, K.; Varadarajan, V. A Review of Maximum Power Point Tracking Algorithms for Wind Energy Conversion Systems. *J. Mar. Sci. Eng.* **2021**, *9*, 1187. [CrossRef]
15. Dahbi, A.; Nait-Said, N.; Nait-Said, M.-S. A novel combined MPPT-pitch angle control for wide range variable speed wind turbine based on neural network. *Int. J. Hydrogen Energy* **2016**, *41*, 9427–9442. [CrossRef]
16. Taoussi, M.; Karim, M.; Hammoumi, D.; el Bekkali, C.; Bossoufi, B.; el Ouanjli, N. Comparative study between Backstepping adaptive and Field-oriented control of the DFIG applied to wind turbines. In Proceedings of the 3rd IEEE International Conference on Advanced Technologies for Signal and Image Processing, Fez, Morocco, 22–24 May 2017.
17. Bouderbala, M.; Bossoufi, B.; Lagrioui, A.; Taoussi, M.; Aroussi, H.A.; Ihedrane, Y. Direct and indirect vector control of a doubly fed induction generator based in a wind energy conversion system. *Int. J. Electr. Comput. Eng. (IJECE)* **2019**, *9*, 1531–1540. [CrossRef]
18. Saady, I.; Karim, M.; Bossoufi, B.; Motahhir, S.; Adouairi, M.S.; Majout, B.; Lamnadi, M.; Masud, M.; Al-Amri, J.F. Optimisation for a photovoltaic pumping system using indirect Field Oriented Control of Induction Motor. *Electronics* **2021**, *10*, 3076. [CrossRef]
19. Tiwari, R.; Kumar, K.; Babu, N.R.; Prabhu, K.R. Coordinated MPPT and DPC Strategies for PMSG based Grid Connected Wind Energy Conversion System. *Energy Procedia* **2018**, *145*, 339–344. [CrossRef]
20. Majout, B.; Bossoufi, B.; Karim, M.; Ouanjli, N.; Saady, I.; Laggoun, Z.; Mahfoud, M.; Yessef, M. Model Reference Adaptive System Based DPC-SVM Control for Permanent Magnet Synchronous Generator. In *Digital Technologies and Applications*; ICDTA 2022: Lecture Notes in Networks and Systems; Motahhir, S., Bossoufi, B., Eds.; Springer: Cham, Switzerland, 2022; Volume 454, pp. 535–544.
21. Mahfoud, M.E.L.; Bossoufi, B.; Ouanjli, N.E.L.; Mahfoud, S.; Taoussi, M. Improved Direct Torque Control of Doubly Fed Induction Motor Using Space Vector Modulation. *Int. J. Intell. Eng. Syst.* **2021**, *14*, 177–188. [CrossRef]
22. Zaihidee, F.M.; Mekhilef, S.; Mubin, M. Robust Speed Control of PMSM Using Sliding Mode Control (SMC)—A Review. *Energies* **2019**, *12*, 1669. [CrossRef]
23. Bossoufi, B.; Karim, M.; Lagrioui, A.; Taoussi, M.; Derouich, A. Observer backstepping control of DFIG-Generators for wind turbines variable-speed: FPGA-based implementation. *Renew Energy* **2015**, *81*, 903–917. [CrossRef]
24. Yang, Z.-J.; Nagai, T.; Kanae, S.; Wada, K. Dynamic surface control approach to adaptive robust control of nonlinear systems in semi-strict feedback form. *Int. J. Syst. Sci.* **2007**, *38*, 709–724. [CrossRef]
25. Ouanjli, N.E.L.; TaoussI, M.; Derouich, A.; Chebabhi, A.; Ghzizal, A.E.L.; Bossoufi, B. High Performance Direct Torque Control of Doubly Fed Induction Motor using Fuzzy Logic. *Gazi Univ. J. Sci. Syst.* **2018**, *31*, 532–542.
26. el Karaoui, I.; Maaroufi, M.; Bossoufi, B. Fuzzy sliding mode power control for wind power generation systems connected to the grid. *IJPEDS Int. J. Power Electron. Drive Syst.* **2022**, *13*, 606–619.
27. Mekrini, Z.; Bri, S.; Bouchnaif, J.; Bossoufi, B. Experimental results of vector control for an asynchronous machine. *TELKOMNIKA (Telecommun. Comput. Electron. Control)* **2020**, *18*, 3285–3292. [CrossRef]
28. Taoussi, M.; Bossoufi, B.; Bouderbala, M.; Motahhir, S.; Alkhammash, E.H.; Masud, M.; ZineLabidine, N.; Karim, M. Implementation and Validation of Hybrid Control for Wind Turbine Using FPGA Controller Board. *Electronics* **2021**, *10*, 3154. [CrossRef]
29. El Ouanjli, N.; Derouich, A.; El Ghzizal, A.; Bouchnaif, J.; Taoussi, M.; Bossoufi, B. Real-time Implementation in dSPACE of DTC-Backstepping for Doubly Fed Induction Motor. *Eur. Phys. J. Plus* **2019**, *135*, 2–9. [CrossRef]

30. Bouderbala, M.; Bossoufi, B.; Deblecker, O.; Alami Aroussi, H.; Taoussi, M.; Lagrioui, A.; Motahhir, S.; Masud, M.; Alraddady, F.A. Experimental Validation of Predictive Current Control for DFIG: FPGA Implementation. *Electronics* **2021**, *10*, 2670. [CrossRef]

31. Orlando, N.A.; Liserre, M.; Mastromauro, R.A.; Dell'Aquila, A. A Survey of Control Issues in PMSG-Based Small Wind-Turbine Systems. *IEEE Trans. Ind. Inform.* **2013**, *9*, 1211–1221. [CrossRef]

32. Majout, B.; Bossoufi, B.; Bouderbala, M.; Masud, M.; Al-Amri, J.F.; Taoussi, M.; El Mahfoud, M.; Motahhir, S.; Karim, M. Improvement of PMSG-Based Wind Energy Conversion System Using Developed Sliding Mode Control. *Energies* **2022**, *15*, 1625. [CrossRef]

33. Zribi, M.; Alrifai, M.; Rayan, M. Sliding Mode Control of a Variable—Speed Wind Energy Conversion System Using a Squirrel Cage Induction Generator. *Energies* **2017**, *10*, 604. [CrossRef]

34. Osman, A.M.; Alsokhiry, F. Sliding Mode Control for Grid Integration of Wind Power System Based on Direct Drive PMSG. *IEEE Access* **2022**, *10*, 26567–26579. [CrossRef]

35. Jena, N.K.; Pradhan, H.; Choudhury, A.; Mohanty, K.B.; Sanyal, S.K. A novel SMC based vector control strategy used for decoupled control of PMSG based variable speed wind turbine system. In Proceedings of the 2017 International Conference on Circuit, Power and Computing Technologies (ICCPCT), Kollam, India, 20–21 April 2017; pp. 1–6.

36. Errami, Y.; Ouassaid, M.; Cherkaoui, M.; Maaroufi, M. SlidingMode Control Scheme of Variable Speed Wind Energy Conversion System Based on the PMSG for Utility Network Connection. In *Advances and Applications in Sliding Mode Control Systems, Studies in Computational Intelligence*, 1st ed.; Azar, A.T., Zhu, Q., Eds.; Springer: Cham, Switzerland, 2015; pp. 167–200.

37. Majout, B.; Abrahmi, D.; Ihedrane, Y.; El Bakkali, C.; Mohammed, K.; Bossoufi, B. Improvement of sliding mode power control applied to wind system based on doubly-fed induction generator. *Int. J. Power Electron. Drive Syst.* **2021**, *12*, 441–452. [CrossRef]

38. Valenciaga, F.; Puleston, P. High-Order Sliding Control for a Wind Energy Conversion System Based on a Permanent Magnet Synchronous Generator. *IEEE Trans. Energy Convers.* **2008**, *23*, 860–867. [CrossRef]

39. Matraji, I.; Al-Durra, A.; Errouissi, R. Design and experimental validation of enhanced adaptive second-order SMC for PMSG-based wind energy conversion system. *Int. J. Electr. Power Energy Syst.* **2018**, *103*, 21–30. [CrossRef]

40. Benbouzid, M.; Beltran, B.; Amirat, Y.; Yao, G.; Han, J.; Mangel, H. Second-order sliding mode control for DFIG-based wind turbines fault ride-through capability enhancement. *ISA Trans.* **2014**, *53*, 827–833. [CrossRef]

41. Shen, X.; Liu, J.; Alcaide, A.M.; Yin, Y.; Leon, J.I.; Vazquez, S.; Wu, L.; Franquelo, L.G. Adaptive Second-Order Sliding Mode Control for Grid-Connected NPC Converters with Enhanced Disturbance Rejection. *IEEE Trans. Power Electron.* **2022**, *37*, 206–220. [CrossRef]

42. Benelghali, S.; El Hachemi Benbouzid, M.; Charpentier, J.F.; AhmedAli, T.; Munteanu, I. Experimental validation of a marine current turbine simulator: Application to a permanent magnet synchronous generator-based system second-order sliding mode control. *IEEE Trans. Ind. Electron.* **2011**, *58*, 118–126. [CrossRef]

43. Phan, D.; Huang, S. Super-Twisting Sliding Mode Control Design for Cascaded Control System of PMSG Wind Turbine. *J. Power Electron.* **2015**, *15*, 1358–1366. [CrossRef]

44. Zholtayev, D.; Rubagotti, M.; Do, T.D. Adaptive super-twisting sliding mode control for maximum power point tracking of PMSG-based wind energy conversion systems. *Renew Energy* **2022**, *183*, 877–889. [CrossRef]

45. Yaichi, I.; Semmah, A.; Wira, P.; Djeriri, Y. Super-twisting Sliding Mode Control of a Doubly-fed Induction Generator Based on the SVM Strategy. *Period. Polytech. Electr. Eng. Comput. Sci.* **2019**, *63*, 178–190. [CrossRef]

46. Swikir, A.; Utkin, V. Chattering analysis of conventional and super twisting sliding mode control algorithm. *Proc. IEEE Int. Work. Var. Struct. Syst.* **2016**, *2016*, 98–102.

47. Shtessel, Y.; Taleb, M.; Plestan, F. A novel adaptive-gain super twisting sliding mode controller: Methodology and application. *Automatica* **2012**, *48*, 759–769. [CrossRef]

48. Li, S.; Zhou, M.; Yu, X. Design and Implementation of Terminal Sliding Mode Control Method for PMSM Speed Regulation System. *IEEE Trans. Ind. Inform.* **2013**, *9*, 1879–1891. [CrossRef]

49. Feng, Y.; Yu, X.; Man, Z. Non-singular terminal sliding mode control of rigid manipulators. *Automatica* **2002**, *38*, 2159–2167. [CrossRef]

50. Jin, M.; Lee, J.; Chang, P.H.; Choi, C. Practical Nonsingular Terminal Sliding-Mode Control of Robot Manipulators for High-Accuracy Tracking Control. *IEEE Trans. Ind. Electron.* **2009**, *56*, 3593–3601.

51. Shi, R.; Zhang, X. Adaptive Fractional-order Non-singular Fast Terminal Sliding Mode Control Based on Fixed Time Observer. *Proc. Inst. Mech. Eng. Part C J. Mech. Eng. Sci.* **2022**, *236*, 7006–7016. [CrossRef]

52. Wang, Y.; Zhu, K.; Yan, F.; Chen, B. Adaptive super-twisting nonsingular fast terminal sliding mode control for cable-driven manipulators using time-delay estimation. *Adv. Eng. Softw. J.* **2019**, *128*, 113–124. [CrossRef]

53. Solis, C.U.; Clempner, J.B.; Poznyak, A.S. Fast terminal sliding mode control with an integral filter applied to a van der pol oscillator. *IEEE Trans. Ind. Electron.* **2017**, *64*, 5622–5628. [CrossRef]

54. Madani, T.; Daachi, B.; Djouani, K. Modular controller design based fast terminal sliding mode for articulated exoskeleton systems. *IEEE Trans. Control. Syst. Technol.* **2016**, *25*, 1133–1140. [CrossRef]

55. Sun, G.; Wu, L.; Kuang, Z.; Ma, Z.; Liu, J. Practical tracking control of linear motor via fractional-order sliding mode. *Automatica* **2018**, *94*, 221–235. [CrossRef]

56. Saravanakumar, R.; Jena, D. Validation of an integral sliding mode control for optimal control of a three blade variable speed variable pitch wind turbine. *Int. J. Electr. Power Energy Syst.* **2015**, *69*, 421–429. [CrossRef]

57. Liu, J.; Zhou, F.; Zhao, C.; Wang, Z. A PI-Type Sliding Mode Controller Design for PMSG-Based Wind Turbine. *Complexity* **2019**, *2019*, 2538206. [CrossRef]

58. Maaruf, M.; El Ferik, S.; Mahmoud, M.S. Integral Sliding Mode Control with Power Exponential Reaching Law for DFIG. In Proceedings of the 17th International Multi-Conference on Systems, Signals & Devices (SSD), Monastir, Tunisia, 20–23 July 2020; pp. 1122–1127.

59. Lin, S.-C.; Chen, Y.-Y. Design of self-learning fuzzy sliding mode controllers based on genetic algorithms. *Fuzzy Sets Syst.* **1997**, *86*, 139–153. [CrossRef]

60. Kharabian, B.; Mirinejad, H. Hybrid Sliding Mode/H-Infinity Control Approach for Uncertain Flexible Manipulators. *IEEE Access* **2020**, *8*, 170452–170460. [CrossRef]

61. Lian, J.; Zhao, J. Robust H-infinity integral sliding mode control for a class of uncertain switched nonlinear systems. *J. Control Theory Appl.* **2010**, *8*, 521–526. [CrossRef]

62. Lin, F.-J.; Chang, C.-K.; Huang, P.-K. FPGA-Based Adaptive Backstepping Sliding-Mode Control for Linear Induction Motor Drive. *IEEE Trans. Power Electron.* **2007**, *22*, 1222–1231. [CrossRef]

63. Rajendran, S.; Jena, D. Backstepping sliding mode control of a variable speed wind turbine for power optimization. *J. Mod. Power Syst. Clean Energy* **2015**, *3*, 402–410. [CrossRef]

64. Shang, L.; Hu, J. Sliding-Mode-Based Direct Power Control of Grid-Connected Wind-Turbine-Driven Doubly Fed Induction Generators Under Unbalanced Grid Voltage Conditions. *IEEE Trans. Energy Convers.* **2012**, *27*, 362–373. [CrossRef]

65. Benbouhenni, H.; Boudjema, Z.; Bizon, N.; Thounthong, P.; Takorabet, N. Direct Power Control Based on Modified Sliding Mode Controller for a Variable-Speed Multi-Rotor Wind Turbine System Using PWM Strategy. *Energies* **2022**, *15*, 3689. [CrossRef]

66. Diab, A.A.Z.; Ahmed, A.A.; Abdelsalam, H.A. Fuzzy-based Adaptive Sliding Mode Control for a Direct-Driven PMSG Wind Energy System. In Proceedings of the 2019 21st International Middle East Power Systems Conference (MEPCON), Cairo, Egypt, 17–19 December 2019; pp. 81–88. [CrossRef]

67. Yin, X.-X.; Lin, Y.-G.; Li, W.; Gu, Y.-J.; Liu, H.-W.; Lei, P.-F. A novel fuzzy integral sliding mode current control strategy for maximizing wind power extraction and eliminating voltage harmonics. *Energy* **2015**, *85*, 677–686. [CrossRef]

68. Saghafinia, A.; Wooi Ping, H.; Nasir Uddin, M. Fuzzy sliding mode control based on boundary layer theory for chattering-free and robust induction motor drive. *Int. J. Adv. Manuf. Technol.* **2014**, *71*, 57–68. [CrossRef]

69. Hong, C.-M.; Huang, C.-H.; Cheng, F.-S. Sliding mode control for variable-speed wind turbine generation systems using artificial neural network. *Energy Procedia* **2014**, *61*, 1626–1629. [CrossRef]

70. Babaie, M.; Al-Haddad, K. ANN Based Model-Free Sliding Mode Control for Grid-Connected Compact Multilevel Converters: An Experimental Validation. In Proceedings of the 2021 IEEE 30th International Symposium on Industrial Electronics (ISIE), Kyoto, Japan, 20–23 June 2021; pp. 1–6.

71. Baek, S.; Baek, J.; Han, S. An Adaptive sliding mode control with effective switching gain tuning near the sliding surface. *IEEE Access* **2019**, *7*, 15563–15572. [CrossRef]

72. Nguyen, T.H.; Nguyen, T.T.; Nguyen, V.Q.; Le, K.M.; Tran, H.N.; Jeon, J.W. An Adaptive Sliding-Mode Controller with a Modified Reduced-Order Proportional Integral Observer for Speed Regulation of a Permanent Magnet Synchronous Motor. *IEEE Trans. Ind. Electron.* **2022**, *69*, 7181–7191. [CrossRef]

73. Yang, B.; Yu, T.; Shu, H.; Zhang, Y.; Chen, J.; Sang, Y.; Jiang, L. Passivity-based sliding-mode control design for optimal power extraction of a PMSG based variable speed wind turbine. *Renew. Energy* **2018**, *119*, 577–589. [CrossRef]

74. Wei, C.; Qiao, W.; Zhao, Y. Sliding-mode observer-based sensorless direct power control of DFIGs for wind power applications. In Proceedings of the IEEE Power & Energy Society General Meeting, Denver, CO, USA, 26–30 July 2015; pp. 1–5.

75. Yang, B.; Yu, T.; Shu, H.; Dong, J.; Jiang, L. Robust sliding-mode control of wind energy conversion systems for optimal power extraction via nonlinear perturbation observers. *Appl. Energy* **2018**, *210*, 711–723. [CrossRef]

76. Kim, H.; Son, J.; Lee, J. A high-speed sliding-mode observer for the sensorless speed control of a PMSM. *IEEE Trans. Ind. Elect.* **2011**, *58*, 4069–4077.

77. Mi, Y.; Fu, Y.; Li, D.; Wang, C.; Loh, P.C.; Wang, P. The sliding mode load frequency control for hybrid power system based on disturbance observer. *Int. J. Electr. Power Energy Syst.* **2016**, *74*, 446–452. [CrossRef]

78. Wang, M.; Wang, H.; Shi, Y.; Shen, M.; Song, J. A modified sliding-mode controller-based mode predictive control strategy for three-phase rectifier. *Int. J. Circuit Theory Appl.* **2020**, *48*, 1564. [CrossRef]

79. Jeeranantasin, N.; Nungam, S. Sliding Mode Control of Three-Phase AC/DC Converters using Exponential Rate Reaching Law. *J. Syst. Eng. Electron.* **2022**, *33*, 210–221. [CrossRef]

80. Mozayan, S.M.; Saad, M.; Vahedi, H.; Fortin-Blanchette, H.; Soltani, M. Sliding Mode Control of PMSG Wind Turbine Based on Enhanced Exponential Reaching Law. *IEEE Trans. Ind. Electron.* **2016**, *63*, 6148–6159. [CrossRef]

81. Fallaha, C.J.; Saad, M.; Kanaan, H.Y.; Al-Haddad, K. Sliding mode robot control with exponential reaching law. *IEEE Trans. Ind. Electron.* **2011**, *58*, 600–610. [CrossRef]

82. El Makrini, I.; Guerrero, C.R.; Lefeber, D.; Vanderborght, B. The Variable Boundary Layer Sliding Mode Control: A Safe and Performant Control for Compliant Joint Manipulators. *IEEE Robot. Autom. Lett.* **2016**, *2*, 187–192. [CrossRef]

83. Ohnishi, T. Three phase PWM converter/inverter by means of instantaneous active and reactive power control. In Proceedings of the IECON '91: 1991 International Conference on Industrial Electronics, Control and Instrumentation, Kobe, Japan, 26 October–1 November 1991; Volume 91, pp. 819–824.

84. Noguchi, T.; Tomiki, H.; Kondo, S.; Takahashi, I. Direct power control of PWM converter without power-source voltage sensors. *IEEE Trans. Ind. Appl.* **1998**, *34*, 473–479. [CrossRef]

85. Nadour, M.; Essadki, A.; Nasser, T. Comparative analysis between PI & backstepping control strategies of DFIG driven by wind turbine. *Int. J. Renew. Energy Resour.* **2017**, *7*, 1307–1316.

86. Razali, A.; Rahman, A.; George, G.; Rahim, N. Analysis and design of new switching look-up table for virtual flux direct power control of grid connected three phase PWM AC-DC converter. *IEEE Trans. Ind. Appl.* **2014**, *51*, 1189–1200. [CrossRef]

87. Zhi, D.; Xu, L.; Williams, B.W. Improved Direct Power Control of Grid-Connected DC/AC Converters. *IEEE Trans. Power Electron.* **2009**, *24*, 1280–1292. [CrossRef]

88. Malinowski, M.; Kazmierkowski, M.P.; Hansen, S.; Blaabjerg, F.; Marques, G.D. Virtualflux-based direct power control of three-phase PWM rectifiers. *IEEE Trans. Ind. Appl.* **2001**, *37*, 1019–1027. [CrossRef]

89. Chaoui, A.; Krim, F.; Gaubert, J.-P.; Rambault, L. DPC controlled three-phase active filter for power quality improvement. *Int. J. Electr. Power Energy Syst.* **2008**, *30*, 476–485. [CrossRef]

90. Cirrincione, M.; Pucci, M.; Vitale, G. Direct power control of three-phase VSIs for the minimization of common-mode emissions in distributed generation systems. *Electr. Power Syst. Res.* **2011**, *81*, 830–839. [CrossRef]

91. Chaoui, A.; Gaubert, J.-P.; Krim, F. Power quality improvement using DPC controlled three-phase shunt active filter. *Electr. Power Syst. Res.* **2010**, *80*, 657–666. [CrossRef]

92. Zhang, Y.; Qu, C. Table-based direct power control for three-phase AC/DC converters under unbalanced grid voltages. *IEEE Trans. Power Electron.* **2015**, *30*, 7090–7099. [CrossRef]

93. Bouafia, A.; Gaubert, J.-P.; Krim, F. Analysis and design of new switching table for direct power control of three-phase PWM rectifier. In Proceedings of the 13th International Power Electronics and Motion Control Conference, Poznan, Poland, 1–3 September 2008; pp. 703–709.

94. Aissaoui, H.E.; Ougli, A.E.; Tidhaf, B. Neural Networks and Fuzzy Logic Based Maximum Power Point Tracking Control for Wind Energy Conversion System. *Adv. Sci. Technol. Eng. Syst. J.* **2021**, *6*, 586–592. [CrossRef]

95. Kwak, S.; Park, J.-C. Model-Predictive Direct Power Control with Vector Preselection Technique for Highly Efficient Active Rectifiers. *IEEE Trans. Ind. Inform.* **2015**, *11*, 44–52. [CrossRef]

96. Kwak, S.; Moon, U.-C.; Park, J.-C. Predictive-Control-Based Direct Power Control with an Adaptive Parameter Identification Technique for Improved AFE Performance. *IEEE Trans. Power Electron.* **2014**, *29*, 6178–6187. [CrossRef]

97. Antoniewicz, P.; Kazmierkowski, M.P. Virtual-Flux-Based Predictive Direct Power Control of AC/DC Converters with Online Inductance Estimation. *IEEE Trans. Ind. Electron.* **2008**, *55*, 4381–4390. [CrossRef]

98. Zhang, Y.; Xie, W.; Li, Z.; Zhang, Y. Model predictive direct power control of a PWM rectifier with duty cycle optimization. *IEEE Trans. Power Electron.* **2013**, *28*, 5343–5351. [CrossRef]

99. Song, Z.; Tian, Y.; Chen, W.; Zou, Z.; Chen, Z. Predictive Duty Cycle Control of Three-Phase Active-Front-End Rectifiers. *IEEE Trans. Power Electron.* **2015**, *31*, 698–710. [CrossRef]

100. Hu, J. Improved Dead-Beat Predictive DPC Strategy of Grid-Connected DC–AC Converters with Switching Loss Minimization and Delay Compensations. *IEEE Trans. Ind. Inform.* **2012**, *9*, 728–738. [CrossRef]

101. Choi, D.; Lee, K.; Member, S. Dynamic performance improvement of AC/DC converter using model predictive direct power control with finite control set. *IEEE Trans. Ind. Electron.* **2015**, *62*, 757–767. [CrossRef]

102. Aurtenechea, S.; Rodríguez, M.; Oyarbide, E.; Torrealday, J.R. Predictive control strategy for DC/AC converters based on direct power control. *IEEE Trans. Ind. Electron.* **2007**, *54*, 1261–1271.

103. Hu, J.; Zhu, Z.Q. Improved voltage-vector sequences on dead-beat predictive direct power control of reversible three-phase grid-connected voltage-source converters. *IEEE Trans. Power Electron.* **2013**, *28*, 254–267. [CrossRef]

104. Song, Z.; Chen, W.; Xia, C. Predictive direct power control for three-phase gridconnected converters without sector information and voltage vector selection. *IEEE Trans. Power Electron.* **2014**, *29*, 5518–5531. [CrossRef]

105. Vazquez, S.; Marquez, A.; Aguilera, R.; Quevedo, D.; Leon, J.I.; Franquelo, L.G. Power control for grid-connected power converters. *IEEE Trans. Ind. Electron.* **2015**, *62*, 2010–2020. [CrossRef]

106. Zhang, Y.; Qu, C. Model predictive direct power control of PWM rectifiers under unbalanced network conditions. *IEEE Trans. Ind. Electron.* **2015**, *62*, 4011–4022. [CrossRef]

107. Cho, Y.; Beum, L.K. Virtual-flux-based direct power control of three-phase PWM rectifiers with fast dynamic response. *IEEE Trans. Ind. Appl.* **2016**, *31*, 3348–3359. [CrossRef]

108. Zhang, Y.; Qu, C. Direct power control of a pulse width modulation rectifier using space vector modulation under unbalanced grid voltages. *IEEE Trans. Power Electron.* **2015**, *30*, 5892–5901. [CrossRef]

109. Fischer, J.R.; Gonz, S.A.; Carugati, I.; Herr, M.A.; Judewicz, M.G.; Carrica, D.O. Robust predictive control of grid-tied converters based on direct power control. *IEEE Trans. Power Electron.* **2014**, *29*, 5634–5643. [CrossRef]

110. Bouafia, A.; Gaubert, J.-P.; Krim, F. Predictive direct power control of three-phase pulsewidth modulation (PWM) rectifier using space vector modulation (SVM). *IEEE Trans. Power Electron.* **2010**, *25*, 228–236. [CrossRef]

111. Restrepo, J.A.; Aller, J.M.; Viola, J.C.; Bueno, A.; Habetler, T.G. Optimum space vector computation technique for direct power control. *IEEE Trans. Power Electron.* **2009**, *24*, 1637–1645. [CrossRef]

112. Tao, Y.K.; Wang, L.; Wu, Q.H.; Tang, W.H. Virtual-flux-based predictive direct power control of three-phase AC/DC converters. In Proceedings of the IEEE PES Asia-Pacific Power and Energy Engineering Conference (APPEEC), Hong Kong, China, 7–10 December 2014; pp. 1–6.

113. Hu, J.; Shang, L.; He, Y.; Zhu, Z.Q. Direct active and reactive power regulation of grid connected DC/AC converters using sliding mode control approach. *IEEE Trans. Power Electron.* **2011**, *26*, 210–222. [CrossRef]

114. Bouafia, A.; Krim, F.; Gaubert, J.-P. Fuzzy-logic-based switching state selection for direct power control of three-phase PWM rectifier. *IEEE Trans. Ind. Electron.* **2009**, *56*, 1984–1992. [CrossRef]

115. Bouafia, A.; Krim, F.; Gaubert, J.-P. Design and implementation of high performance direct power control of three-phase PWM rectifier, via fuzzy and PI controller for output voltage regulation. *Energy Convers. Manag.* **2009**, *50*, 6–13. [CrossRef]

116. Portillo, R.; Vazquez, S.; Leon, J.I.; Prats, M.M.; Franquelo, L.G. Model based adaptive direct power control for three-level NPC converters. *IEEE Trans. Ind. Inform.* **2013**, *9*, 1148–1157. [CrossRef]

117. Vazquez, S.; Sanchez, J.A.; Carrasco, J.M.; Leon, J.I.; Galvan, E. A model-based direct power control for three-phase power converters. *IEEE Trans. Ind. Electron.* **2008**, *55*, 1647–1657. [CrossRef]

118. Malinowski, M.; Jasin, M.; Kazmierkowski, M.P. Simple direct power control of three phase PWM rectifier using space-vector modulation (DPC-SCM). *IEEE Trans. Ind. Electron.* **2004**, *51*, 447–454. [CrossRef]

119. Escobar, G.; Stankovic, A.M.; Carrasco, J.M.; Galvan, E.; Ortega, R. Analysis and design of direct power control (DPC) for a three phase synchronous rectifier via output regulation subspaces. *IEEE Trans. Power Electron.* **2003**, *18*, 823–830. [CrossRef]

120. Zhang, Y.; Li, Z.; Zhang, Y.; Xie, W.; Piao, Z.; Hu, C. Performance improvement of direct power control of PWM rectifier with simple calculation. *IEEE Trans. Power Electron.* **2013**, *28*, 3428–3437. [CrossRef]

121. Suul, J.A.; Luna, A.; Rodríguez, P.; Undeland, T. Virtual-flux-based voltage-sensor-less power control for unbalanced grid conditions. *IEEE Trans. Power Electron.* **2012**, *27*, 4071–4087. [CrossRef]

122. Malinowski, M.; Marques, G. New direct power control of three-phase PWM boost rectifiers under distorted and imbalanced line voltage conditions. In Proceedings of the International Symposium on Industrial Electronics, Rio de Janeiro, Brazil, 9–11 June 2003; pp. 438–443.

123. Nian, H.; Shen, Y.; Yang, H.; Quan, Y. Flexible grid connection technique of voltage source inverter under unbalanced grid conditions based on direct power control. *IEEE Trans. Ind. Appl.* **2015**, *51*, 4041–4050. [CrossRef]

124. Eloy-Garcia, J.; Arnaltes, S.; Rodriguez-Amenedo, J.L. Extended direct power control of a three-level neutral point clamped voltage source inverter with unbalanced voltages. In Proceedings of the IEEE Power Electronics Specialists Conference, Rhodes, Greece, 15–19 June 2008; pp. 3396–3400.

125. Komatsu, Y.; Kawaba, T. A control method of active power filter in unsymmetrical voltage system. In Proceedings of the International Conference on Power Electronics and Drive Systems, Singapore, 26–29 May 1997; pp. 839–843.

126. Malinowski, M. Sensorless Control Strategies for Three-Phase PWM Rectifiers. Ph.D. Thesis, Politechnika Warszawska, Warszawa, Poland, 2001.

127. Norniella, J.G.; Cano, J.M.; Orcajo, G.A.; Rojas, C.H.; Pedrayes, J.F.; Cabanas, M.F.; Melero, M.G. Improving the dynamics of virtual-flux-based control of three-phase active rectifiers. *IEEE Trans. Ind. Electron.* **2014**, *61*, 177–187. [CrossRef]

128. Shan, D.-l.; Song, S.-z.; Ma, J.-w.; Wang, X.-b. Direct power control of PWM rectifiers based on virtual flux. In Proceedings of the International Conference on Computer Application and System Modeling, Taiyuan, China, 22–24 October 2010; pp. 613–616.

129. Bouafia, A.; Gaubert, J.P.; Chaoui, A. Direct power control scheme based on disturbance rejection principle for three-phase PWM AC/DC converter under different input voltage conditions. *J. Electr. Syst.* **2012**, *4*, 367–383.

130. Hu, J.; Zhu, Z.Q. Investigation on switching patterns of direct power control strategies for grid-connected DC-AC converters based on power variation rates. *IEEE Trans. Power Electron.* **2011**, *26*, 3582–3598. [CrossRef]

131. Chen, B.S.; Joos, G. Direct power control of active filters with averaged switching frequency regulation. *IEEE Trans. Power Electron.* **2008**, *23*, 2729–2737. [CrossRef]

132. Gong, B.; Wang, K.; Zhang, J.; You, J.; Luo, Y.; Zhang, W. Advanced switching table for direct power control of a three-phase PWM rectifier. In Proceedings of the IEEE Conference and Expo Transportation Electrification Asia-Pacific, Beijing, China, 31 August–3 September 2014; pp. 1–5.

133. Baktash, A.; Vahedi, A.; Masoum, M.A.S. Improved switching table for direct power control of three-phase PWM rectifier. In Proceedings of the 2007 Australasian Universities Power Engineering Conference, Perth, Australia, 9–12 December 2007; Volume 2, pp. 592–596.

134. Zhang, Y.; Peng, Y.; Qu, C. Comparative study of model predictive control and direct power control for PWM rectifiers with active power ripple minimization. In Proceedings of the IEEE Energy Conversion Congress and Exposition (ECCE), Montreal, QC, Canada, 20–24 September 2015; pp. 3823–3830.

135. Li, P.; Xiong, L.; Wu, F.; Ma, M.; Wang, J. Sliding mode controller based on feedback linearization for damping of sub-synchronous control interaction in DFIG-based wind power plants. *Int. J. Electr. Power Energy Syst.* **2019**, *107*, 239–250. [CrossRef]

136. Drhorhi, I.; El Fadili, A.; Berrahal, C.; Lajouad, R.; El Magri, A.; Giri, F.; Azar, A.T.; Vaidyanathan, S. Chapter 11—Adaptive backstepping controller for DFIG-based wind energy conversion system. In *Advances in Nonlinear Dynamics and Chaos (ANDC), Backstepping Control of Nonlinear Dynamical Systems*; Vaidyanathan, S., Azar, A.T., Eds.; Academic Press: Cambridge, MA, USA, 2021; pp. 235–260, ISBN 9780128175828.

137. Ghamrasni, M.E.L.; Mahmoudi, H.; Bossoufi, B. Modelling and simulation of a wind system using variable wind regimes with Backstepping control of DFIG. *IOP Conf. Ser. Earth Environ. Sci.* **2018**, *161*, 012026. [CrossRef]

138. Shen, X.; Xie, T.; Wang, T. A Fuzzy Adaptative Backstepping Control Strategy for Marine Current Turbine under Disturbances and Uncertainties. *Energies* **2020**, *13*, 6550. [CrossRef]

139. Roy, T.K.; Mahmud, M.A.; Islam, S.N.; Oo, A.M.T. Nonlinear Adaptive Backstepping Controller Design for Permanent Magnet Synchronous Generator (PMSG)-Based Wind Farms to Enhance Fault Ride Through Capabilities. In Proceedings of the 2019 IEEE Power & Energy Society General Meeting (PESGM), Atlanta, GA, USA, 4–8 August 2019; pp. 1–5. [CrossRef]

140. Mahersi, E.; Khedher, A. Backstepping flux observer for nonlinear control of the direct-drive permanent magnet synchronous generator wind turbines. *Wind Eng.* **2016**, *40*, 540–554. [CrossRef]

141. Liu, Y.-H. Adaptive dynamic surface asymptotic tracking for a class of uncertain nonlinear systems. *Int. J. Robust Nonlinear Control* **2017**, *28*, 1233–1245. [CrossRef]

142. Min, W.; Liu, Q. An improved adaptive fuzzy backstepping control for nonlinear mechanical systems with mismatched uncertainties. *Automatika* **2019**, *60*, 1–10. [CrossRef]

143. Shuai, S.; Baoyong, Z.; Xiaona, S.; Zhengqiang, Z. Adaptive neuro-fuzzy Backstepping dynamic surface control for uncertain fractional-order nonlinear systems. *Neurocomputing* **2019**, *360*, 172–184.

144. Xue, G.; Lin, F.; Li, S.; Liu, H. Adaptive fuzzy finite-time backstepping control of fractional-order nonlinear systems with actuator faults via command-filtering and sliding mode technique. *Inf. Sci.* **2022**, *600*, 189–208. [CrossRef]

145. Wang, F.; Guo, Y.; Wang, K.; Zhang, Z.; Hua, C.; Zong, Q. Disturbance observer based robust backstepping control design of flexible air-breathing hypersonic vehicle. *IET Control Theory Appl.* **2019**, *13*, 572–583. [CrossRef]

146. Hui, J.; Ling, J.; Gu, K.; Yuan, J. Adaptive backstepping controller with extended state observer for load following of nuclear power plant. *Prog. Nucl. Energy* **2021**, *137*, 103745. [CrossRef]

147. Kim, Y.; Park, T.; Lee, J.M. Integration of model predictive control and backstepping approach and its stability analysis. *IFAC-PapersOnLine* **2018**, *51*, 405–410. [CrossRef]

148. Nizami, T.K.; Chakravarty, A. Neural Network Integrated Adaptive Backstepping Control of DC-DC Boost Converter. *IFAC-PapersOnLine* **2020**, *53*, 549–554. [CrossRef]

149. El-Sousy, F.F.M.; El-Naggar, M.F.; Amin, M.; Abu-Siada, A.; Abuhasel, K.A. Robust Adaptive Neural-Network Backstepping Control Design for High-Speed Permanent-Magnet Synchronous Motor Drives: Theory and Experiments. *IEEE Access* **2019**, *7*, 99327–99348. [CrossRef]

150. Bossoufi, B.; Karim, M.; Taoussi, M.; Aroussi, H.A.; Bouderbala, M.; Deblecker, O.; Motahhir, S.; Nayyar, A.; Alzain, M.A. Rooted Tree Optimization for the Backstepping Power Control of a Doubly Fed Induction Generator Wind Turbine: dSPACE Implementation. *IEEE Access* **2021**, *9*, 26512–26522. [CrossRef]

151. Makhad, M.; Zazi, M.; Loulijat, A.; Simon, A.O. Robust Integral Backstepping control for Optimal Power Extraction of a PMSG-based Variable Speed Wind Turbines. In Proceedings of the 1st International Conference on Innovative Research in Applied Science, Engineering and Technology (IRASET), Meknes, Morocco, 16–19 April 2020; pp. 1–6.

152. Armghan, H.; Yang, M.; Wang, M.; Ali, N.; Armghan, A. Nonlinear integral backstepping based control of a DC microgrid with renewable generation and energy storage systems. *Int. J. Electr. Power Energy Syst.* **2019**, *117*, 105613. [CrossRef]

153. Loucif, M.; Mechernene, A.; Bossoufi, B. Integral Backstepping Power Control of DFIG Based Nonlinear Modeling Using Voltage Oriented Control. In Proceedings of the Springer-ICDTA'2021 the International Conference on Digital Technologies and Applications, Fez, Morocco, 29–30 January 2021.

154. Prasad, N.V.D.V.E.; Sahani, M.; Dash, P.K. A new adaptive integral back stepping fractional order sliding mode control approach for PV and wind with battery system based DC microgrid. *Sustain. Energy Technol. Assess.* **2022**, *52*, 102261. [CrossRef]

155. Belkhier, Y.; Achour, A. An intelligent passivity-based backstepping approach for optimal control for grid-connecting permanent magnet synchronous generator-based tidal conversion system. *Int. J. Energy Res.* **2021**, *45*, 5433–5448. [CrossRef]

156. Zu, H.; Zhang, G.-B.; Fei, S.-M. Enhanced model reference adaptive backstepping control of permanent magnet synchronous generator equipped wind energy conversion system with stator parameters varying. In Proceedings of the 2011 Chinese Control and Decision Conference (CCDC), Mianyang, China, 23–25 May 2011; pp. 133–138.

157. Bossoufi, B.; Karim, M.; Taoussi, M.; Aroussi, H.A.; Bouderbala, M.; Motahhir, S.; Camara, M.B. DSPACE-based implementation for observer backstepping power control of DFIG wind turbine. *IET Electr. Power Appl.* **2020**, *14*, 2395–2403. [CrossRef]

158. Bossoufi, B.; Karim, M.; Lagrioui, A. MATLAB & Simulink simulation with FPGA Based Implementation adaptative and not adaptative backstepping nonlinear control of a permanent magnet synchronous machine drive. *WSEAS Trans. Syst. Control* **2014**, *9*, 86–100.

159. Rajendran, S.; Jena, D. Backstepping Sliding Mode Control for variable speed wind turbine. In Proceedings of the 2014 Annual IEEE India Conference (INDICON), Pune, India, 11–13 December 2014; pp. 1–6.

160. Mourabit, Y.E.L.; Derouich, A.; Ghzizal, A.E.L.; Bouchnaif, J.; Ouanjli, N.E.L.; Zamzoum, O.; Mezioui, K.; Bossoufi, B. Implementation and validation of Backstepping control for PMSG wind turbine using dSPACE controller board. *Energy Rep. J.* **2019**, *5*, 807–821.

161. Polinder, H.; Ferreira, J.; Jensen, B.; Abrahamsen, A.; Atallah, K.; McMahon, R. Trends in wind turbine generator systems. *IEEE J. Emerg. Sel. Top. Power Electron.* **2013**, *1*, 174–185. [CrossRef]

162. Bossoufi, B.; Lagrioui, A. High Performance Predictive Control for Permanent Magnet Synchronous Machine Drive: FPGA-Based Im-plementation. In Proceedings of the Springer-ICDTA'2021 the International Conference on Digital Technologies and Applications, Fez, Morocco, 29–30 January 2021.

163. Yaramasu, V.; Wu, B.; Sen, P.C.; Kouro, S.; Narimani, M. High-power wind energy conversion systems: State-of-the-art and emerging technologies. *Proc. IEEE* **2015**, *103*, 740–788. [CrossRef]

164. Polinder, H.; van der Pijl, F.; de Vilder, G.-J.; Tavner, P. Comparison of direct-drive and geared generator concepts for wind turbines. *IEEE Trans. Energy Convers.* **2006**, *21*, 725–733. [CrossRef]

165. Li, H.; Chen, Z.; Polinder, H. Optimization of Multibrid Permanent-Magnet Wind Generator Systems. *IEEE Trans. Energy Convers.* **2009**, *24*, 82–92. [CrossRef]

166. Liserre, M.; Cardenas, R.; Molinas, M.; Rodríguez, J. Overview of multi-MW wind turbines and wind parks. *IEEE Trans. Ind. Electron.* **2011**, *58*, 1081–1095. [CrossRef]

167. Yang, X.; Patterson, D.; Hudgins, J. Permanent magnet generator design and control for large wind turbines. In Proceedings of the IEEE Symposium on Power Electronics and Machines in Wind Applications (PEMWA), Denver, CO, USA, 16–18 July 2012; pp. 1–5.

168. Zhong, L.; Rahman, M.; Hu, W.; Lim, K. Analysis of direct torque control in permanent magnet synchronous motor drives. *IEEE Trans. Power Electron.* **1997**, *12*, 528–536. [CrossRef]

169. Geyer, T. A Comparison of Control and Modulation Schemes for Medium-Voltage Drives: Emerging Predictive Control Concepts Versus PWM-Based Schemes. *IEEE Trans. Ind. Appl.* **2011**, *47*, 1380–1389. [CrossRef]

170. Rodriguez, J.; Kennel, R.M.; Espinoza, J.R.; Trincado, M.; Silva, C.A.; Rojas, C.A. High-Performance Control Strategies for Electrical Drives: An Experimental Assessment. *IEEE Trans. Ind. Electron.* **2012**, *59*, 812–820. [CrossRef]

171. Chivite-Zabalza, J.; Girones, C.; Carcar, A.; Larrazabal, I.; Olea, E.; Zabaleta, M. Comparison of power conversion topologies for a multi-megawatt off-shore wind turbine, based on commercial power electronic building blocks. In Proceedings of the IEEE Industrial Electronics Conference (IECON), Vienna, Austria, 10–13 November 2013; pp. 5242–5247.

172. Yazdani, A.; Iravani, R. A Neutral-Point Clamped Converter System for Direct-Drive Variable-Speed Wind Power Unit. *IEEE Trans. Energy Convers.* **2006**, *21*, 596–607. [CrossRef]

173. Faulstich, A.; Stinke, J.; Wittwer, F. Medium voltage converter for permanent magnet wind power generators up to 5 MW. In Proceedings of the European Conference on Power Electronics and Applications (EPE), Dresden, Germany, 11–14 September 2005; p. 9.

174. Alepuz, S.; Calle, A.; Busquets-Monge, S.; Kouro, S.; Wu, B. Use of Stored Energy in PMSG Rotor Inertia for Low-Voltage Ride-Through in Back-to-Back NPC Converter-Based Wind Power Systems. *IEEE Trans. Ind. Electron.* **2013**, *60*, 1787–1796. [CrossRef]

175. Rodriguez, J.; Bernet, S.; Steimer, P.K.; Lizama, I.E. A Survey on Neutral-Point-Clamped Inverters. *IEEE Trans. Ind. Electron.* **2010**, *57*, 2219–2230. [CrossRef]

176. Kouro, S.; Malinowski, M.; Gopakumar, K.; Pou, J.; Franquelo, L.G.; Wu, B.; Rodriguez, J.; Perez, M.A.; Leon, J.I. Recent Advances and Industrial Applications of Multilevel Converters. *IEEE Trans. Ind. Electron.* **2010**, *57*, 2553–2580. [CrossRef]

177. Blaabjerg, F.; Ma, K. Future on power electronics for wind turbine systems. *IEEE J. Emerg. Sel. Top. Power Electron.* **2013**, *1*, 139–152. [CrossRef]

178. Preindl, M.; Bolognani, S. Model predictive direct torque control with finite control set for PMSM drive systems, Part 1: Maximum torque per ampere operation. *IEEE Trans. Ind. Inform.* **2013**, *9*, 1912–1921. [CrossRef]

179. Nguen, H.T.; Al Sumaiti, A.S.; Al Hosani, K.; El Moursi, M.S. Multifunctional Control of Wind Turbine Based Nano-Grid Connected to Distroted Utility-Grid. *IEEE Trans. Power Syst.* **2021**, *37*, 576–589. [CrossRef]

180. Bouderbala, M.; Bossoufi, B.; Aroussi, H.A.; Taoussi, M.; Lagrioui, A. Novel deadbeat predictive control strategy for DFIG's back to back power converter. *IJPEDS Int. J. Power Electron. Drive Syst.* **2022**, *13*, 2731–2741. [CrossRef]

181. Bouderbala, M.; Bossoufi, B.; Lagrioui, A.; Taoussi, M.; Aroussi, H.A.; Livinti, P. DEADBEAT Control Applied to Wind Power System. In Proceedings of the 5th International Conference on Renewable Energies for Developing Countries—REDEC, Marrakech, Morocco, 25–26 June 2020.

182. Balamurugan, A.; Baskaran, P. Load Usage Self Regulating Control of Dynamic Response of the Grid Tied Wind Power Generator under Unbalanced Non-Linear Load. *J. Green Eng.* **2020**, *10*, 13688–13697.

183. Shehata, E.G.; Thomas, J. Simple Model Predictive Control of High Power Direct-Driven PMSG Wind Energy Systems. In Proceedings of the 2021 22nd IEEE International Conference on Industrial Technology (ICIT), Valencia, Spain, 10–12 March 2021; Volume 1, pp. 482–487.

184. Prince, M.K.K.; Arif, M.T.; Gargoom, A.; Oo, A.M.T.; Haque, E. Modeling, Parameter Measurement, and Control of PMSG-based Grid-connected Wind Energy Conversion System. *J. Mod. Power Syst. Clean Energy* **2021**, *9*, 1054–1065. [CrossRef]

185. Cortes-Vega, D.; Ornelas-Tellez, F.; Anzurez-Marin, J.; Cordova-Aguilar, C. Optimal tracking control for a Permanent Magnet Synchronous Generator. In Proceedings of the 2019 6th International Conference on Control, Decision and Information Technologies (CoDIT), Paris, France, 23–26 April 2019; pp. 691–696.

186. Yip, S.Y.; Che, H.S.; Tan, C.P.; Chong, W.T. A lookup table model predictive direct torque control of permanent-magnet synchronous generator based on Vienna rectifier. *IEEE J. Emerg. Sel. Top. Power Electron.* **2019**, *8*, 1208–1222. [CrossRef]

187. El Alami, H.; Bossoufi, B.; Motahhir, S.; Alkhammash, E.H.; Masud, M.; Karim, M.; Taoussi, M.; Bouderbala, M.; Lamnadi, M.; El Mahfoud, M. FPGA in the Loop Implementation for Observer Sliding Mode Control of DFIG-Generators for Wind Turbines. *Electronics* **2021**, *11*, 116. [CrossRef]

188. Mohammed, E.M.; Badre, B.; Najib, E.O.; Abdelilah, H.; Houda, E.A.; Btissam, M.; Said, M. Predictive Torque and Direct Torque Controls for Doubly Fed Induction Motor: A Comparative Study. In Proceedings of the International Conference on Digital Technologies and Applications, Fez, Morocco, 28–30 January 2021; Springer: Cham, Switzerland, 2021; pp. 825–835.

189. Bossoufi, B.; Lagrioui, A. Speed Control for PMSM Drive System Using Predictive Control. *J. Autom. Syst. Eng. JSAE* **2017**, *11*, 208–221.

190. Yaramasu, V.; Wu, B.; Chen, J. Model-Predictive Control of Grid-Tied Four-Level Diode-Clamped Inverters for High-Power Wind Energy Conversion Systems. *IEEE Trans. Power Electron.* **2013**, *29*, 2861–2873. [CrossRef]

191. Laggoun, Z.E.Z.; Khalile, N.; Benalla, H. A Comparative study between DPC-SVM and PDPC-SVM. In Proceedings of the International Conference on Advanced Electrical Engineering (ICAEE), Algiers, Algeria, 19–21 November 2019; pp. 1–5. [CrossRef]

192. Rivera, M.; Yaramasu, V.; Rodriguez, J.; Wu, B. Model Predictive Current Control of Two-Level Four-Leg Inverters—Part II: Experimental Implementation and Validation. *IEEE Trans. Power Electron.* **2013**, *28*, 3469–3478. [CrossRef]

193. Yaramasu, V.; Wu, B.; Rivera, M.; Rodriguez, J. Enhanced model predictive voltage control of four-leg inverters with switching frequency reduction for standalone power systems. In Proceedings of the IEEE 15th International Power Electronics and Motion Control Conference (EPE/PEMC), Novi Sad, Serbia, 4–6 September 2012; pp. 1–5.

194. Laggoun, Z.E.Z.; Benalla, H.; Nebti, K. A Power Quality Enhanced for the Wind Turbine with Sensorless Direct Power Control under Different Input Voltage Conditions. *Electr. Eng. Electromech.* **2021**, *16*, 64–71. [CrossRef]

195. Chai, S.; Wang, L.; Rogers, E. Model predictive control of a permanent magnet synchronous motor with experimental validation. *Control. Eng. Pract.* **2013**, *21*, 1584–1593. [CrossRef]

196. Zhang, G.; Gao, L.; Yang, H.; Mei, L. A novel method of model predictive control on permanent magnet synchronous machine with Laguerre functions. *Alex. Eng. J.* **2021**, *60*, 5485–5494. [CrossRef]

197. Barros, J.D.; Silva, J.F.A.; Jesus, É.G. Fast-predictive optimal control of NPC multilevel converters. *IEEE Trans. Ind. Electron.* **2012**, *60*, 619–627. [CrossRef]

198. Bolognani, S.; Bolognani, S.; Peretti, L.; Zigliotto, M. Design and implementation of model predictive control for electrical motor drives. *IEEE Trans. Ind. Electron.* **2008**, *56*, 1925–1936. [CrossRef]

199. Schwenzer, M.; Ay, M.; Bergs, T.; Abel, D. Review on model predictive control: An engineering perspective. *Int. J. Adv. Manuf. Technol.* **2021**, *117*, 1327–1349. [CrossRef]

200. Vazquez, S.; Leon, J.I.; Franquelo, L.G.; Rodriguez, J.; Young, H.A.; Marquez, A.; Zanchetta, P. Model Predictive Control: A Review of Its Applications in Power Electronics. *IEEE Ind. Electron. Mag.* **2014**, *8*, 16–31. [CrossRef]

201. Lagrioui, A.; Mahmoudi, H.; Bossoufi, B. Discrete linear predictive control of permanent magnet synchronous motor (pmsm). *J. Theor. Appl. Inf. Technol.* **2011**, *31*, 21–28.

202. Bossoufi, B.; Karim, M.; Ionita, S.; Lagrioui, A. Nonlinear non adaptive backstepping with sliding-mode torque control approach for pmsm motor. *J. Electr. Syst.* **2012**, *8*, 236–248.

203. Bossoufi, B.; Karim, M.; Lagrioui, A.; Taoussi, M.; EL Hafyani, M.L. Backstepping control of DFIG Generators for Wide-Range Variable-Speed Wind Turbines. *Int. J. Autom. Control* **2014**, *8*, 122–140. [CrossRef]

204. Bossoufi, B.; Karim, M.; Lagrioui, A.; Taoussi, M.; Derouich, A. Adaptive Backstepping Control of DFIG Generators for Wide-Range Variable-speed Wind Turbines system. *J. Electr. Syst.* **2014**, *10*, 317–330.

205. Barara, M.; Bennassar, A.; Abbou, A.; Akherraz, M.; Bossoufi, B. Advanced Control of Wind Electric Pumping System for Isolat-ed Areas Application. *Int. J. Power Electron. Drive Syst.* **2014**, *4*, 66–77.

206. Xiao, F.; Zhang, Z.; Yin, X. Fault Current Characteristics of the DFIG under Asymmetrical Fault Conditions. *Energies* **2015**, *8*, 10971–10992. [CrossRef]

207. Song, Z.; Xia, C.; Liu, T. Predictive current control of three-phase grid-connected converters with constant switching frequency for wind energy systems. *IEEE Trans. Ind. Electron.* **2013**, *60*, 2451–2464. [CrossRef]

208. Rivera, M.; Wilson, A.; Rojas, C.A.; Rodríguez, J.; Espinoza, J.R.; Wheeler, P.W.; Empringham, L. A comparative assessment of model predictive current control and space vector modulation ina direct matrix converter. *IEEE Trans. Ind. Electron.* **2013**, *60*, 578–588. [CrossRef]

209. Sun, X.; Wu, M.; Lei, G.; Guo, Y.; Zhu, J. An Improved Model Predictive Current Control for PMSM Drives Based on Current Track Circle. *IEEE Trans. Ind. Electron.* **2021**, *68*, 3782–3793. [CrossRef]